Cohesin forms fountains at active enhancers in *C. elegans*

Bolaji N. Isiaka[1,2], Jennifer I. Semple[1], Anja Haemmerli[1], Saurabh Thapliyal[3], Klement Stojanovski[6], Moushumi Das[1,2], Nick Gilbert[3], Dominique A. Glauser[4], Benjamin Towbin[6], Daniel Jost[5] and Peter Meister[1] *

[1] Cell Fate and Nuclear Organization, Institute of Cell Biology, University of Bern, Switzerland
[2] Graduate School for Cellular and Biomedical Sciences, University of Bern, Switzerland
[3] MRC Human Genetics Unit, Institute of Genetics and Cancer, The University of Edinburgh
[4] Department of Biology, University of Fribourg, Fribourg Switzerland
[5] Laboratoire de Biologie et Modélisation de la Cellule, Ecole Normale Supérieure de Lyon, CNRS, UMR5239, Inserm U1293, Université Claude Bernard Lyon 1 France
[6] Institute of Cell Biology, University of Bern, Switzerland

[*] correspondence to peter.meister@unibe.ch

Abstract

Transcriptional enhancers must find their target genes both efficiently and specifically. Chromatin conformation capture revealed the critical function of three-dimensional chromosome segmentation by topologically associated domains (TADs) to limit the search space of enhancers for promoters in mammals. In nematodes, although more than 30’000 sequences with characteristic enhancer chromatin features have been identified, the autosomal genome is not segmented by TADs, raising the question of the mechanism directing enhancer-promoter specificity. Using high-resolution HiC, we show that enhancer loci correlate with 3D hairpin-like structures extending 10-50 kb from the enhancers, hereafter designated as fountains. Fountains are specific to active enhancers, accumulate the major somatic cohesin and disappear when the latter is cleaved *in vivo*. Fountains accumulate topological constraints and are enriched for topoisomerases and the negatively-supercoiled DNA binder psoralen. Short-term topoisomerase depletion leads to small-scale structural changes at the fountain tip. Functionally, fountain disappearance correlates with enhancer-proximal gene activation, suggesting fountains play a similar role as TADs and direct enhancer-promoter interactions, in particular for genes expressed in neurons. We directly observe this cell-type specific upregulation for the *skn-1/Nrf* gene in a pair of head neurons. Phenotypically, cohesin cleavage has a major impact on nematode movement and foraging attitudes, demonstrating that changes in neuronal gene expression impact nervous system function, reminiscent of pathologies caused by cohesin mutations in humans. Together, this study highlights a clear link between 3D genome organization at enhancers by cohesin, transcriptional gene regulation and animal behavior.

Introduction

Gene transcription is tightly regulated by a combination of promoter-proximal elements and more distant enhancer sequences. Enhancers increase the transcription of target genes by recruiting sequence-specific transcription factors, which in turn attract additional proteins to facilitate transcription. Notably, enhancers are capable of activating transcription independently of their location relative to their target gene, and can act at large distances from the promoter, up to several tens of kilobases in mammals (Karpinska & Oudelaar, 2023).

Recent chromosome conformation capture studies in mammals have shown that enhancer and target promoter are often located in the same megabase-sized three-dimensional domain known as a topologically associated domain (TAD) while TAD segmentation regulates promoter/enhancer contacts and the downstream transcriptional regulation (Dixon et al., 2012; Rinzema et al., 2022; Zuin et al., 2022). The formation of TADs is the result of chromatin looping, whereby cohesin extrudes chromatin until it reaches sequence elements bound by the DNA-binding protein CTCF (for review Pueschel et al., 2016).

In *C. elegans,* two different studies identified between 19’000 and 30’000 sequences with enhancer-type chromatin features (Fig. 1AB for L3 stage enhancers; (Daugherty et al., 2017; Jänes et al., 2018). These sequences exhibit an open chromatin structure (ATAC-seq peaks), characteristic histone marks (high H3K4 monomethylation coupled to low H3K4 trimethylation), short-stretch bidirectional transcription, and enrichment for initiator sequence element (Inr) (Daugherty et al., 2017; Jänes et al., 2018). A limited number of these sequences were individually tested for their capacity to activate a minimal promoter driving GFP independently of their location relative to the promoter. This confirmed that these sequences are *bona fide* enhancers leading to cell- and developmental stage-specific expression of the transgene. It is currently unclear how the activity of these enhancers is limited to their target genes, as unlike mammals, nematodes do not harbor TADs on their autosomes, and no CTCF homolog or functional homolog has been identified in the *C. elegans* genome. Additionally, no nematode boundary elements have been described to date, and during interphase, cohesin is replaced by condensin I as the primary long-range loop extruder (Das et al., 2022). These observations suggest that cohesin function is largely divergent in nematodes compared to mammals and that an alternative mechanism to TADs regulates enhancer-promoter contacts and the ensuing gene expression. Hereafter, we show that nematode enhancers are insulated in small-scale 3D structures which we call fountains, created by cohesin activity. Cohesin^{COH-1} cleavage leads to upregulation of active enhancer- and fountain-proximal genes, in particular genes expressed in neurons. Strikingly, cohesin^{COH-1} cleavage leads to a breadth of behavioral changes, linking 3D genome

organization by cohesin, neuronal gene expression and nervous system function in animal behavior.

Results

Enhancer loci correlate with 3D fountains

To assess whether enhancers would colocalize with specific three-dimensional genomic features, we generated average chromatin conformation capture contact maps for third larval stage animals centered on enhancer sequences (Das et al., 2022; Daugherty et al., 2017; Jänes et al., 2018). These contact maps revealed a clear and distinct enlarged second diagonal perpendicular to the main HiC diagonal, extending several kilobases from the enhancers (Fig. 1AB). These increased contact probabilities between the enhancers and neighboring sequences are indicative of the formation of a loose hairpin structure centered on the enhancer sequences, resulting in the alignment of two branches of the hairpin (Fig. 1G). Hereafter, we call these structures fountains.

In one of the studies above, enhancers were further characterized using ChromHMM genome segmentation (Daugherty et al., 2017). This division classified enhancers into active enhancers covered with H3K4me1, repressed enhancers with no specific histone mark, and H3K27me3 enhancers covered with H3K27me3, deposited by the PRC2 Polycomb complex (Fig. 1A). When we averaged the contact maps of these different enhancer types, we observed that active enhancers were associated with fountains, whereas repressed enhancers did not show any fountains, and H3K27me3-covered enhancers showed a decrease of expected contacts in the second diagonal, as well as a cross-like high contact probability feature, suggesting that H3K27me3 enhancers cluster together *in vivo* (Fig. 1A). Similarly, when we segmented the second enhancer dataset (Jänes et al., 2018) based on the same ChromHMM chromatin states, we made almost identical observations: active enhancers were associated with fountains, while either repressed or trimethylated H3K27-covered enhancers were not (Fig. 1B).

In previous ChIP studies, a set of genomic regions bound by multiple transcription factors were identified, named Highly Occupied Target (HOT) sites (Chen et al., 2014; Gerstein et al., 2010). As enhancers are binding sites for transcription factors, HOT sites and enhancers often co-occur on nearby loci. To investigate whether HOT sites, active enhancers, or both types of sequence elements colocalize with fountains, we created average contact maps centered on HOT sites that either overlapped with active enhancers or were distinct from them. Our results indicate that HOT sites only correlated with fountains (Fig. 1CD) when these overlapped with active enhancers. In contrast, HOT sites not overlapping with active

enhancers did not create fountains, while active enhancers not overlapping with HOT sites did (Fig. 1CD).

We next wondered whether fountains would be stage-specific, by selecting enhancers active in embryos and inactive in the third larval stage, or conversely. We calculated average chromatin conformation contact maps for these different enhancer sets at different stages using our HiC data of third larval stage and HiC data performed with the same protocol in embryos (Das et al., 2022; Jimenez et al., 2021). For both enhancer sets, we observed clear fountains in their respective developmental stages (Fig. 1E). In contrast, no fountains could be observed for enhancers active in embryos using larvae HiC maps, and larvae-specific enhancers created smaller and weaker fountains in embryonic HiC data (Fig. 1E). The latter might be due to the fact that mixed stage embryos were used to perform chromatin conformation, in which a variable proportion of animals are already in late developmental stages during which some larval enhancers are already active. We conclude that fountain formation is stage-specific, in agreement with the activity of the enhancers.

Finally, we explored whether fountains were unique to enhancers or if they were associated with other open chromatin regions such as active transcription start sites (TSS). The worm genome is highly compact and enhancers are located only a couple kilobases away from their putative target promoters (Daugherty et al., 2017; Jänes et al., 2018). To examine TSS-specific 3D structures, we calculated the average contact maps of the bottom or top 20 % of all expressed genes ranked by expression level. We found no evidence of fountain formation in the bottom 20 %, while the 20 % most expressed genes showed very limited fountain formation (Fig. 1F), vastly smaller than the fountains observed at active enhancers (Fig. 1AB). In summary, our data shows that fountain formation is a feature specific to active enhancers and not selectively associated with transcribed genes or HOT sites. We envision fountains as loose hairpin-like structures with the active enhancer sitting at the tip of the fountains (Fig. 1G).

Enhancers are binding sites for cohesin^{COH-1}

Recent studies have described similar structures orthogonal to the diagonal in bacteria (Brandão et al., 2019), T cells (Guo et al., 2022) and zebrafish sperm (Wike et al., 2021) as well as during zygotic genome activation in zebrafish (Galitsyna et al., 2023). These structures are thought to be formed through bidirectional loop extrusion by SMC complexes repeatedly loaded at defined loci (in our case, the active enhancers). Nematodes express four types of SMC complexes in the soma: canonical condensin I and II, and two variants of cohesin, differing by their kleisin subunit, SCC-1 or COH-1. We previously demonstrated that condensin I performs long-range loop extrusion during interphase (>100 kb), while condensin II has no clear interphasic function (Das et al, 2022). Cohesin^{SCC-1} is involved in

sister chromatid cohesion during mitosis and exclusively expressed in dividing cells (Mito et al., 2003). Early immunofluorescence studies show that COH-1 is expressed in all cells, suggesting cohesin^{COH-1} is the major interphasic cohesin. In our previous study, we confirmed that the common SMC-1 subunit of cohesin is expressed ubiquitously at high levels (Das et al., 2022 and Fig. 2A), suggesting cohesin^{COH-1} is present in most, if not all cells. We used publicly available ChIP-seq data (Gerstein et al., 2010) to determine whether enhancer sequences were enriched for cohesin^{COH-1}. Cohesin^{COH-1} is specifically enriched in a broad region centered on active enhancers, extending several kilobases away from the enhancer itself (Fig. 2B, upper part, red line and heatmap). In contrast, repressed enhancers had only a small enrichment limited to the enhancer sequences. Cohesin^{COH-1} was slightly depleted on H3K27me3 enhancers compared to neighboring sequences (Fig. 2B, upper part, blue line).

To investigate whether cohesin^{COH-1} enrichment on active enhancers correlated with the size of the fountains, we classified active enhancers into 5 classes based on their cohesin^{COH-1} enrichment and created average contact frequency maps for each class. Our analysis revealed that enhancers with high cohesin^{COH-1} enrichment generated large fountains extending several tens of kilobases away from the enhancer locus (Fig. 2B, right side), while active enhancers of the second-to-lowest quintile formed very small fountains and active enhancers of the lowest quintile did not correlate with fountains.

To directly investigate the role of cohesin^{COH-1}, we made use of our previously described inducible cleavage system for the cohesin kleisins COH-1 and/or SCC-1 (Crawley et al., 2016). When protease expression was induced during the first larval stage (three hours after diapause exit), cleavage of COH-1, but not SCC-1 caused the disappearance of most GFP-tagged SMC-1 (Das et al., 2022 and Fig. 2C), indicating that COH-1 cleavage leads to the degradation of the entire cohesin^{COH-1} complex and that cohesin^{COH-1} is the major cohesin isoform. We calculated average contact maps centered on active enhancers in control animals and upon cleavage of either or both cohesin kleisins. Cleavage of SCC-1 only marginally modified contact maps, in contrast to the cleavage of COH-1, in which fountains were almost completely absent (Fig. 2DE). Similar results were obtained upon simultaneous cleavage of COH-1 and SCC-1 (Fig. 2D). Cohesin^{COH-1} is thereby necessary for the maintenance of fountains at active enhancers. Given the loop extrusion activity of cohesin, the most likely model for the formation of the fountains is the specific loading of the cohesin complex at active enhancers followed by bidirectional loop extrusion randomly stopping on either side, as suggested by polymer modeling (Galitsyna et al., 2023) supplementary file 1).

The effects of cohesin^{COH-1} cleavage can be visualized by creating contact-ratio maps between cleaved and control contact maps (Fig. 2F, ratio from the two conditions in E). We used these ratio maps to locate fountains genome-wide by filtering the diagonal of the HiC map with a model-based kernel similar to the average fountain (see Fig. S1 and Methods).

We found 1263 fountains equally distributed across the chromosomes, with 95 % (1196 out of 1263) overlapping with annotated active enhancers and only 6 % and 14 % overlapping with silent and H3K27me3 enhancers, respectively (72 and 172 fountains; (Daugherty et al., 2017). This suggests that identified fountains on the differential HiC maps and dependent on cohesin^{COH-1} are primarily associated with active enhancers. The apparent discrepancy with the enhancer annotations may be due to the lower resolution of the HiC data (2 kb) compared to enhancers (1 bp). Furthermore, we found that chromatin states at fountain origin bins as well as those of the neighboring bins were enriched for enhancer states compared to genome-wide coverage (Fig. 2G), supporting the notion that fountains are related to enhancer activity. Notably, some fountains were asymmetric, with more contacts on one side than on the other, implying that loop extrusion by cohesin^{COH-1} might be directionally biased in those cases (Fig. 2H). Asymmetry correlated with differential transcription levels between the two sides of the fountains, with more transcription on the side where the fountains were the longest (Fig. S2A). Fountain disappearance upon COH-1 cleavage did not affect this asymmetry in relative transcription levels (Fig. S2B). Similarly, enhancer states were asymmetrically distributed and more abundant on the side where fountains were the longest (Fig. S2C). Together, this suggests that asymmetric transcription levels and/or enhancer state abundance are a cause rather than a consequence of fountain asymmetry, possibly by being more permissive to loop extrusion by cohesin^{COH-1}.

Enhancers are bound by topoisomerases

To further understand fountain formation, we examined published ChIP-seq data at enhancer sequences acquired at the same third larval developmental stage (Morao et al., 2022). Bidirectional transcription at enhancers results in the production of short transcripts, and as expected, RNA polymerase II is enriched at enhancer sequences. In contrast to cohesin^{COH-1}, which extends several kilobases away from the enhancer itself along the entire length of the fountains, RNA polymerase II is only enriched at the tip of the fountains (Fig. 3AB; (Jänes et al., 2018; Morao et al., 2022). Interestingly, we found that the enrichment of RNA polymerase II at active enhancers correlated with the abundance of COH-1 (Spearman correlation coefficient R=0.63), which in turn determined fountain sizes (Fig. 2B). These findings prompted us to explore the interplay between enhancer transcription and fountain formation.

During transcription, the opening of the double helix and movement of the RNA polymerase generates negative supercoils behind the polymerase, and in the case of divergent transcription at enhancers, negative supercoils accumulate between the two polymerases progressing in opposite directions. In front of the polymerases, positive supercoils are generated, in other words, on either side of the transcribed enhancer sequences.

Topoisomerases, the enzymes which relax supercoils by cleaving and unwinding DNA, are therefore expected to be present at enhancers. Indeed, a clear, specific and correlated enrichment for both TOP-1 and TOP-2 was observed at active enhancers (Fig. 3C, R=0.83). Additionally, for both topoisomerases, the enrichment correlated with cohesin^{COH-1} abundance (R=0.6 and 0.59, respectively). As for RNA polymerase II, the TOP-1 and TOP-2 ChIP-seq signal was limited to the enhancer sequences at the tip of the fountains. These findings suggest that topoisomerases are regulating the supercoiling at enhancer sequences created by repeated small-stretch transcription. To directly test whether enhancer sequences are indeed negatively supercoiled, we performed biotinylated psoralen crosslinking followed by sequencing (bTMP-seq; (Naughton et al., 2013). In brief, nuclei were extracted, incubated with bTMP and crosslinked to DNA using long-wavelength UV irradiation. Crosslinked DNA was then purified using biotin pulldown and sequenced. As TMP has a differential affinity for T/A-rich sequences, pulldowns were normalized to purified DNA crosslinked *in vitro*. As for topoisomerases, bTMP was enriched in the middle of the fountains at active enhancer sequences, demonstrating that these sequences are negatively supercoiled *in vivo* (Fig. 3D).
To further investigate the role of topoisomerases in the maintenance of fountains, we created average contact frequency maps centered on active enhancers from published topoisomerase depletion data (Fig. 3E; (Morao et al., 2022). As for our data, average contact maps in control animals showed clear fountains (Fig. 3E, TIR1 control). Upon depletion of either TOP-1 or TOP-2, fountains were only mildly affected and changes impacted mostly the tip of the fountains which shows a high enrichment for both enzymes (Fig. 3C and E, TOP-1^{AID}, TOP-2^{AID}, inset). TOP-1 depletion led to a slight increase in contacts along the trunk of the fountain, while the contacts on either side of the active enhancers were slightly reduced. Conversely, TOP-2 depletion resulted in a slight decrease in contacts along the fountain trunk, with a limited increase in contacts on either side of the active enhancers (Fig. 3E, TOP-1^{AID}, TOP-2^{AID}, difference maps to TIR1 control). We conclude that short-term depletion of either TOP-1 or TOP-2 has only a marginal effect on fountains, mainly at the tip.
To further characterize the role of transcription in fountain maintenance, we blocked transcription for five hours using α-amanitin. We investigated first whether transcription inhibition was accompanied by altered supercoiling by performing bTMP-seq and plotted the average enrichment at different enhancer types upon α-amanitin treatment (Fig. 3G, 25 kb (top) and 6 kb (bottom) windows centered on enhancers). As expected, since transcription inhibition would decrease supercoiling, α-amanitin treatment lowered bTMP enrichment on all enhancer types, more strikingly at the H3K27me3 enhancers, although the reason for this remains unclear. At active enhancers, bTMP enrichment was decreased at the enhancers but slightly higher on either side of them, suggesting that the absence of transcription would lead to the relocation of negative supercoils away from the enhancer sequences, but not

completely abolish these. Additionally, we performed HiC upon transcription inhibition and created average contact maps centered on active enhancers. Similarly to topoisomerase depletion, α-amanitin treatment only slightly decreased fountain strength (Fig. 3F, difference map to control). Collectively, our findings lead us to the conclusion that fountains are enriched for RNA polymerase II, topoisomerases and bTMP, indicating probable DNA supercoiling. However, the presence of either RNA polymerases or topoisomerases is not essential for the maintenance of the fountains, indicating that these structures remain stable for at least one hour without topoisomerases and four hours without transcription once they are formed.

Cohesin^{COH-1} cleavage correlates with transcriptional activation of genes close to active enhancers and fountains

We previously analyzed the transcriptional consequences of COH-1 cleavage in entire animals (Das *et al.* 2022). Analyzing this data in isolation with less stringent filtering criteria, 895 genes were significantly up-regulated, and 993 genes were significantly down-regulated ($p<0.05$). Most changes in transcript abundance were small, with only 98 up- and 52 down-regulated genes with a fold change larger than 1.41 ($|log2FC|>0.5$). As ATAC-seq, modified histone ChIP-seq and RNA-seq are made on entire animals with a large number of different cell types, the target genes for enhancers have not been determined directly for almost all enhancers (Daugherty et al., 2017; Jänes et al., 2018). We therefore distributed genes into six categories by assigning each enhancer to the closest TSS (or to none if the gene was not the closest TSS to any enhancer). “Active”, “Repressed”, “H3K27me3-repressed” categories were TSS of genes closest to only one type of enhancer; “Mixed active and repressed” category were TSS of genes closest to a mixture of enhancers from the active and either of the two categories - H3K27me3 or repressed; and “mixed repressed” were genes closest to a mixture of “repressed” and “H3K27me3-repressed” enhancers. We then analyzed the impact of COH-1 cleavage on these different gene categories (Fig. 4A). When no enhancer was present in the vicinity of the gene (the largest number of genes), average expression after cleavage of COH-1 was slightly lower than in the control experiment. For genes proximal to mixed or active enhancers, the change in expression levels of these genes was biased towards higher expression (Fig. 4A). In contrast, genes proximal to H3K27-methylated enhancers were evenly distributed between up- and down-regulated. Therefore, genes close to active enhancers were upregulated upon COH-1 cleavage, suggesting fountain formation limits active enhancer activity. The fact that genes close to a mixture of active and repressed enhancers and even a mixture of the two repressed categories were also biased towards upregulation, suggests a role for COH-1 in

regulating complex transcriptional landscapes, though the number of genes in these groups is small.

We next analyzed transcriptional changes upon COH-1 cleavage based on the location of the detected fountains (Fig. 2F). For this, we first measured the distance between genes and the closest fountain and split genes based on their transcriptional modulation upon COH-1 cleavage. We found that the average distance to fountains of non-changing or down-regulated genes was not significantly different (Fig. 4B), while upregulated genes were significantly closer to fountains. Second, we focused on the 2 kb bins of the HiC contact map in which the fountain was detected ("fountain bins") and a set of "control bins" located at the midpoint of neighboring fountain bins (Fig. 4C). Genes that overlap fountain bins were significantly biased towards upregulation whereas genes overlapping control bins were equally distributed between up and down regulation (Fig. 4D, similar result with all expressed genes - data not shown). Together, this strongly suggests that fountain ablation by COH-1 cleavage leads to upregulation of fountain-proximal genes. Additionally, genes overlapping fountain bins were more complex than genes overlapping control bins: they had a significantly greater number of transcripts, TSSs and Transcription End Sites (TES) per gene, a larger number of exons, and both their average and maximum transcript length was greater (Fig. 4E), again indicating that COH-1 could be necessary for the regulation of complex transcriptional landscapes.

Enhancers are believed to drive cell-type specific expression, and indeed putative nematode enhancers whose activity was individually tested in animals show cell-type specific expression (Daugherty et al., 2017; Jänes et al., 2018). We reasoned that if COH-1 cleavage led to mild upregulation of genes proximal to active enhancers, this might be due to cell-type specific expression of the latter genes, as RNA-seq is performed on entire animals. Small overall changes would be observed even if transcription levels in individual cells experience major modulation if these genes are expressed only in a few cells per animal. To interrogate whether genes with changed expression levels would belong to a specific cell type, we used the Wormbase Tissue Enrichment Analysis tool to analyze the list of significantly up and down regulated genes (Angeles-Albores et al., 2016). This tool allows to determine in which cell type a gene set is most likely expressed. Genes upregulated upon COH-1 cleavage showed a striking enrichment for neuronal cell types, as well as GO terms and phenotypes associated with neurons (Fig. S3). In contrast, downregulated genes were associated with a range of non-neuronal tissues and core cellular and metabolic processes (Fig. S3). Altogether, this strongly suggests that genes upregulated upon COH-1 cleavage are expressed in neurons.

We next sought strains in which transcription factors were endogenously tagged and located either close or inside a fountain region, in particular transcription factors expressed in

neuronal cell types. *skn-1/Nrf* is such a gene, as it lies between two fountains (Fig. 2EF). In RNA-seq data, *skn-1* shows a modest but significant 1.15 fold upregulation upon COH-1 cleavage compared to TEV control. *skn-1* expression has been widely studied, due to its function in lifespan regulation (for review Blackwell et al., 2015). SKN-1 is a transcription factor with three isoforms named A to C, arising as a result of the use of different promoters and alternative splicing of the transcripts (Fig. 4F). At the third larval stage, the *skn-1c* isoform was undetectable by RNA-seq, hence we focused on *skn-1a* and *skn-1b*. SKN-1A is present in intestinal cells and normally located in the cytoplasm due to its membrane targeting signal at the N-terminus of the protein. Upon stress, SKN-1A relocates to the nucleus for gene regulation (Lehrbach & Ruvkun, 2016; Tullet et al., 2008). In contrast, SKN-1B is exclusively nuclear and solely expressed in two head neurons called ASI (Fig. 4G, TEV control; (Tataridas-Pallas et al., 2021). At the genomic level, *skn-1a* and *skn-1b* share several exons on the 3' part of the gene, but transcription of the two isoforms is controlled by different promoters. Several active enhancers around the *skn-1* gene have been independently identified by two studies in entire animals (Daugherty et al., 2017; Jänes et al., 2018). One of these enhancers is located between the first and the second exon of *skn-1a*, although it remains unclear in which cells this enhancer is active (Fig. 4F, red square). Using a C-terminally GFP-tagged construct which labels all SKN-1 isoforms, we observed that in control animals at the L3 stage, most fluorescence was indeed visible in the nuclei of two ASI neurons, since the diffuse cytoplasmic expression in the intestine is not clearly visible above the autofluorescence of the gut granules, as expected from previous studies (Fig. 4G, TEV control; (Teuscher & Ewald, 2018). The exclusively nuclear fluorescence in ASI identifies SKN-1B as the expressed isoform in these neurons. Upon COH-1 cleavage, a clear increase of the GFP signal was scored, in line with the *skn-1* upregulation which we observed by RNA-seq. Additionally, we detected the accumulation of the GFP-tagged protein in the cytoplasm, filling the entire cell including the sensory axons located in front of the cell body as well as the laterally extending dendrite (Fig. 4G, cohesin^{COH-1} cleavage). This cytoplasmic localization of SKN-1 in ASI neurons has never been observed previously (pers. comm. K. Blackwell, Harvard Medical School). To further assess the nature of the *skn-1* isoform, we took advantage of the stress-mediated nuclear relocation of SKN-1A. We heat-shocked the animals a first time at the L1 stage to induce COH-1 cleavage, and a second time at the L3 stage, 30 minutes before imaging. Under those conditions, no cytoplasmic fluorescence was present, as expected upon relocation of SKN-1A to the nucleus upon stress activation (Fig. 4G, cohesin^{COH-1} cleavage + heat-shock). Differential expression analysis of *skn-1* isoforms at the transcript level showed that *skn-1a* was indeed upregulated (p=0.02), though the downregulation of the more lowly expressed *skn-1b* isoform was not significant (Fig. 4H). We conclude that cleavage of the cohesin^{COH-1}

has dual effects: it upregulates *skn-1* expression and induces significant changes in the isoforms expressed. Specifically, there is a transition in promoter usage from *skn-1b* to *skn-1a*, resulting in the production of the non-neuronal protein SKN-1A. These findings suggest that the cohesin^{COH-1}-mediated formation of fountains can direct promoter use, most likely by restricting active enhancers activity.

COH-1 cleavage minimally delays animal growth and development

To further assess the function of cohesin, we measured the impact of COH-1 cleavage on animal growth during larval development with a time resolution of 10 minutes (Stojanovski, Großhans, et al., 2022) Fig. S4A). COH-1 cleavage led to a small difference in animal volume compared to TEV control (Fig. S4BC). However, this difference was minor compared to previously characterized mutants (*eat-2*, *dbl1*, *raga-1; (Stojanovski, Großhans, et al., 2022)*. We conclude that COH-1 cleavage and fountains disappearance has a minimal effect on animal growth.

COH-1 cleavage has a pleiotropic impact on animal behavior

Since neuronal gene expression is disturbed by COH-1 cleavage, we wanted to analyze its impact on nervous system function using computer-assisted high-content behavioral quantification of worm crawling behavior (Javer et al., 2018). We compared 47 core postural and locomotion parameters in wild type (N2), TEV control and upon cohesin^{COH-1} cleavage. Animals either dwelled on food or were in search of food after 6 h of deprivation (Fig. 5). We found that COH-1 cleavage affected many behavioral parameters in both conditions, whereas the behavior of TEV control animals was indistinguishable from that of wild type (Fig. S5). Some behavioral differences were quite obvious (Fig. 5A and Supplementary Movie 1 and 2). These broad behavioral differences cause animals with cleaved COH-1 to localize at distinctive locations when plotting principal component (PC) scores after a principal component analysis (PCA) (PC1/PC2 space, Fig. 5B). Among the most salient features, COH-1 cleavage caused a striking increase in the body curvature of both fed and starved animals (Fig 5A and E) and impaired the ability of worms to implement food search behavior upon food deprivation (Fig. 5CDFG). In wild type, the entry into the food search locomotion state involves multiple coordinated behavioral changes (Flavell et al., 2020; Thapliyal et al., 2023). These include a marked elevation of animal speed and of the frequency of reorientation events called omega turns (Fig 5CD). As a consequence, worms produce relatively twisted trajectories (Fig. 5F) but disperse fast, dramatically increasing worm displacement as compared to fed animals (Fig. 5G). The up-regulation of both speed and omega turn frequency upon food-deprivation was strongly reduced by COH-1 cleavage (FIg. 5CD), which impaired dispersal (Fig. 5FG). In contrast, TEV cleavage control animals

behaved essentially like wild type (Fig 5A-G). Collectively, these results demonstrate that the post-developmental cleavage of COH-1 produces a pleiotropic impact on worm locomotion and are in line with a model in which COH-1-dependent fountain formation is essential for normal neuronal gene expression and the ensuing proper function of the nervous system.

Discussion

At least three SMC complexes create looping domains on nematode chromosomes

In mammals, cohesin is the main loop extruder acting on interphasic chromosomes and its removal leads to the disappearance of many 3D structures including loops and TADs (Rao et al., 2017; Schwarzer et al., 2017; Wutz et al., 2017). This study, combined with our previous data, demonstrates that at least three different SMC complexes are at play on nematode chromosomes (Das et al., 2022). On the one hand, large-scale chromosome looping is achieved by condensin I creating loops larger than 100 kilobases, while a variant of condensin I specifically targeted to the X chromosome creates specific loop domains resembling TADs on this chromosome (Crane et al., 2015). On the other hand, cohesin^{COH-1} achieves short-patch loop extrusion in the tens of kilobase range centered on active enhancers, giving rise to fountains. This is markedly different from Vertebrates, in which different SMC complexes extrude loops during different cell cycle stages, with cohesins and condensins active during interphase and mitosis, respectively (Golfier et al., 2020). In nematodes, the presence of different interphasic structures maintained by cohesin^{COH-1} or condensin I is unique, suggesting the simultaneous activity of these complexes, which has not been previously observed in Metazoan species.

Peculiar to nematodes of the *Caenorhabditis* genus, two divergent copies of the cohesin kleisins are present in somatic cells (as well as three additional ones in the germline). Early reports suggest that the two somatic kleisins play different roles, as cohesin^{COH-1} is present in somatic cells independently of the cell cycle phase while cohesin^{SCC-1} is exclusively expressed in dividing cells (Mito et al., 2003; Pasierbek et al., 2001). Together with previous work in which we tested the mitotic function of the different SMC complexes, our data demonstrate a functional specialization of the two somatic cohesin complexes: cohesin^{SCC-1} holds sister chromatids together during mitosis, in line with the observed *scc-1* mutant phenotypes due to chromosome segregation defects in dividing cells (Das et al., 2022; Mito et al., 2003). In contrast, cohesin^{COH-1} has a minor role in sister chromatid cohesion, although COH-1 is the most abundant somatic kleisin (Das et al., 2022). Here we show that the function of cohesin^{COH-1} is interphase chromatin loop extrusion, leading to the formation of enhancer fountains. This separation of function between the two cohesin complexes allows to untangle the mitotic and interphasic functions of cohesin.

Nematode enhancers correlate with fountain 3D structures

Enhancers play a critical role in transcriptional gene regulation, conferring cell type and development specificity to gene expression, yet their activity needs to be reined in to avoid unwanted activation of non-target promoters (Karpinska & Oudelaar, 2023). This is achieved in Vertebrates by the formation of TADs created by the interplay between loop extrusion by cohesin and boundary elements bound by CTCF. These 3D chromatin domains limit the search space of enhancers for promoters, thereby reducing enhancer-promoter contact probability and the likelihood of promoter activation (Zuin et al., 2022). Numerous high-resolution chromatin conformation capture data in nematodes failed to identify TADs on autosomes, leaving open the question of how enhancers are spatially restricted to their target promoters (Anderson et al., 2019; Bian et al., 2020; Crane et al., 2015; Das et al., 2022; J. Kim et al., 2022; Morao et al., 2022). Here we present evidence for the existence of 20-50 kb-sized loose hairpin structures centered on active enhancers, similar to flares/hinges, plumes, or jets described in other organisms (Guo et al., 2022; Liu et al., 2021; Wike et al., 2021). The presence of H3K27ac, a marker of enhancer activity, at the focal points of these structures in zebrafish sperm and during fish zygotic genome activation (Galitsyna et al., 2023), as well as in WAPL/CTCF-depleted mESCs or primary thymocytes, suggests that fountains are evolutionarily conserved 3D genome structures.

In thymocytes, jets' projection angle depends on the presence of and distance to CTCF barrier elements, resulting in asymmetric loop extrusion and obstruction of jet elongation. As jets, nematode fountains can be asymmetrical (Fig. 2H), yet there is no CTCF encoded in the nematode genome, nor any described functional homolog of CTCF. This suggests the existence of alternative barriers to and/or more favorable environments for loop extrusion. Transcription may play a role as genes located on the most-extruded side of the asymmetric fountains show a significantly higher expression than genes located on the other side (Fig. S2). This difference between enhancer sides is more likely to be the cause of fountain asymmetry than a consequence of asymmetric fountain formation as removal of fountains by COH-1 cleavage did not change transcription level asymmetry. Conversely, transcription inhibition did not significantly modify asymmetric fountains. Chromatin enhancer states are also enriched on the most-extruded side of the fountains, suggesting that these states might be more permissive to loop extrusion. Similar interplay between transcription and loop extrusion has been observed in Bacteria and WAPL/CTCF-depleted mammalian cells, where loop extrusion is impeded by polymerases, while SMC complexes might be pushed by transcribing complexes (Banigan et al., 2022; Brandão et al., 2019; Rivosecchi et al., 2021; Tran et al., 2017).

Our analysis of published RNA polymerase II and topoisomerases ChIP-seq data showed that active enhancers are enriched for these factors (Fig. 3BC; (Morao et al., 2022). RNA

polymerase enrichment was expected at bidirectionally transcribed active enhancers and topoisomerases enrichment suggest the presence of supercoiled DNA (Jänes et al., 2018). Indeed, our bTMP mapping highlighted a specific enrichment at active enhancers, suggesting the presence of negatively supercoiled DNA (Fig. 3D). Similar to condensin, it is plausible that cohesin's loop extrusion activity at active enhancers leading to fountain formation causes in addition the formation of supercoils and/or plectonemes. Fountains may also restrict the dissipation of torsional stress generated by enhancer transcription or by the loop extrusion activity of cohesin loaded onto enhancers (Davidson et al., 2019).

Degron-mediated degradation of topoisomerases I or II only slightly modified fountain strength (Fig. 3E). Topoisomerase I depletion led to increased contacts at the fountain tip - the active enhancer locus - and a general increase of fountain strength, suggesting that topoisomerase I activity leads to slightly more compact fountains. In contrast, topoisomerase II leads to less contacts along the fountain trunk, suggesting a more relaxed or extended fountain structure. Transcription inhibition using α-amanitin generally slightly weakened fountains, but did not ablate them. Fountains maintenance therefore appear largely independent of topoisomerase activity or transcription, suggesting that once set up, fountains no longer need transcription to remain stable.

Fountains appear functionally similar to TADs

Our results provide evidence for a direct correlation between fountain formation and transcription regulation by enhancers: cohesin^{COH-1} cleavage and subsequentfountain disappearance is accompanied by the upregulation of genes in close proximity to fountains and active enhancers as well as a switch in transcript isoforms (Fig. 4). This strongly suggests that fountains act as suppressors of active enhancer activity, and the downregulation of genes following COH-1 cleavage is an indirect consequence. Consequently, fountains serve as miniature TADs, effectively limiting short-range interactions between active enhancer and non-target promoters located nearby. The compact structure of fountains is well adapted to accommodate the high gene density of the *C. elegans* genome. Our findings align with the observed inhibition of transcription caused by repeated passage of cohesin induced by artificial targeted loading in mammalian cells (Han et al., 2023).

Given that all RNA-seq, HiC and ATAC-seq data were generated from entire animals comprising various tissues, assigning specific enhancers to particular genes remains a challenging task that necessitates individual testing. Nonetheless, our experiments unequivocally demonstrate that genes overlapping with fountains exhibit greater complexity, characterized by multiple TSS, TES and/or exons. The integrity of cohesin^{COH-1} and the

presence of fountains emerge as critical factors in regulating these complex genes, as shown by the isoform switch observed for *skn-1* (Fig. 4E-G).

Cohesin-mediated gene regulation is evolutionarily conserved

Remarkably, our investigation revealed a noteworthy upregulation of genes associated with neuronal function following cohesin^{COH-1} cleavage (Fig. S3). This conserved role of cohesin in interphase neuronal gene regulation transcends species boundaries. In *Drosophila*, cleavage of the cohesin kleisin in post-mitotic neurons results in impaired axonal and dendritic pruning, as well as abnormal larval locomotion (Pauli et al., 2008). Similarly, in humans, mutations in cohesin or cohesin-associated genes have been implicated in cohesinopathies, a group of neurodevelopmental disorders (Kline et al., 2018). The most well-known of these conditions is Cornelia de Lange syndrome (CdLS), associated with mutations in NIPBL or other SMC complex subunits (Cheng et al., 2020; Parenti & Kaiser, 2021).

In nematodes, cleavage of COH-1 and subsequent loss of cohesin^{COH-1} produced a spectrum of behavioral phenotypes (Fig. 5, S4). Notably, in the absence of food, the animals exhibited altered foraging behavior, displaying sluggish movement instead of active foraging (Fig. 5). This finding is reminiscent of genetic screens in nematodes that identified mutations in the *mau-2* gene (MAternally affected Uncoordination (*mau*)). *mau-2* mutants display defects in axon guidance leading to behavioral phenotypes (Takagi et al., 1997) and the gene gave its name to the mice and human Scc4/MAU2 gene necessary for cohesin function. Our study strongly suggests that the observed *mau-2* phenotypes in nematodes are a consequence of cohesin^{COH-1} malfunction in neurons. Similarly, the global dysregulation of genes observed in human CdLS patients further supports the connection to cohesinopathies (Fujita et al., 2017; Parenti & Kaiser, 2021; Robles-Rebollo et al., 2022). Comparison of genes modulated in post-mortem brain neurons of CdLS patients with transcripts modulated upon cohesin^{COH-1} cleavage in nematodes revealed a significant overlap for upregulated genes (Fig. S6; (Weiss et al., 2021). The nematode orthologs of genes upregulated in CdLS were enriched among genes upregulated upon COH-1 cleavage (Fig. S6C), whereas the orthologs of downregulated transcripts in CdLS patients did not display the same pattern (Fig. S6B). Collectively, these similarities strongly indicate that cohesin plays a role in regulating gene expression levels in neurons, most likely through the formation of 3D insulating structures. Nevertheless, further comprehensive studies are required to systematically characterize dysregulated neuronal genes and assess neuronal function upon cohesin^{COH-1} cleavage in *C. elegans*.

In summary, our study provides compelling evidence establishing cohesin^{COH-1} as the key interphase cohesin in *C. elegans*, with a crucial involvement in neuronal function, possibly

through the formation of insulating 3D structures at active enhancers. Leveraging the extensive repertoire of genetic tools available in nematodes, further exploration of cohesin^{COH-1} holds great promise as a genetically tractable model for investigating human cohesinopathies.

Acknowledgements

We would like to thank Cihan Elcin, Laurence Bulliard et Lisa Schild for technical help, Dr. Pamela Nicholson and her team at the NGS platform of the University of Bern, the Meister laboratory for discussion. Some data were acquired on machines supported by the Microscopy Imaging Center (MIC) of the University of Bern. Some strains were provided by the CGC, which is funded by NIH Office of Research Infrastructure Programs (P40 OD010440). This work was funded by the Swiss National Science Foundation 31003A_176226/310030_212472 (to PM), PCEFP3_181204 (to BT), 10030_197607, BSSGI0_155764 and PP00P3_150681(to DAG), the University of Bern and Fribourg, the Agence Nationale pour la Recherche (ANR-18-CE45-0022-01 to DJ), the Wellcome Trust (to NG) and the Novartis Foundation for Medical/Biological Research (to PM).

Figure and legends

Isiaka et al., Figure 1

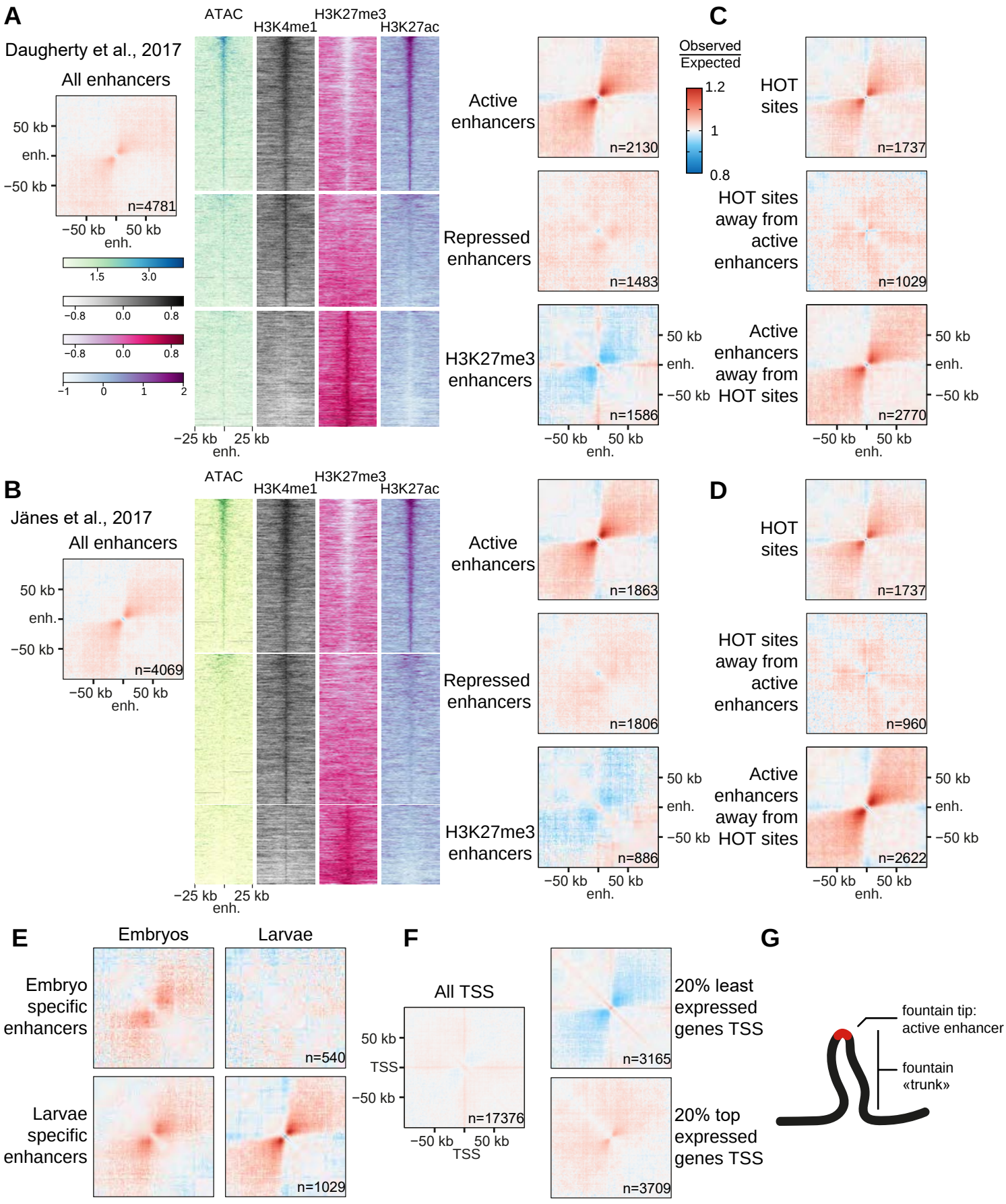

Figure 1. Active enhancers colocalize with loose 3D hairpins structures or fountains. **A.** Average contact frequency maps centered on annotated enhancers from Daugherty et al., highlighting the formation of 3D structures. Further segmentation into active, repressed and H3K27me3-covered enhancers highlight the specificity of fountains for active enhancers. **B.** Average contact frequency maps centered on annotated putative enhancers (all stages) from Jänes et al., further segmented using histone marks as in Daugherty et al. **C,D.** Highly Occupied Target (HOT) sites are not forming fountains. Average contact frequency maps for all HOT sites, for HOT sites located more than 6 kb away from active enhancers and for active enhancers located more than 6 kb away from HOT sites, using active enhancers from Daugherty et al. (C) or Jänes et al. (D). **E.** Fountains for active enhancers are specific for their developmental stage. Average contact maps for embryo-specific and L3 larvae-specific ATAC-seq peaks (ATAC-seq peaks in the top 3 deciles at the considered stage and in the bottom 3 deciles at the other stage). **F.** Transcription start sites (TSS) do not colocalize with fountains. Average contact frequency maps centered on all TSS, and TSS segmented by gene expression. Small fountains present in the most expressed 20 % genes are most likely due to active enhancers located in the vicinity of the TSS. **G.** Cartoon of a typical fountain, with the active enhancer located at the tip of the loose hairpin structure.

Isiaka et al., Figure 2

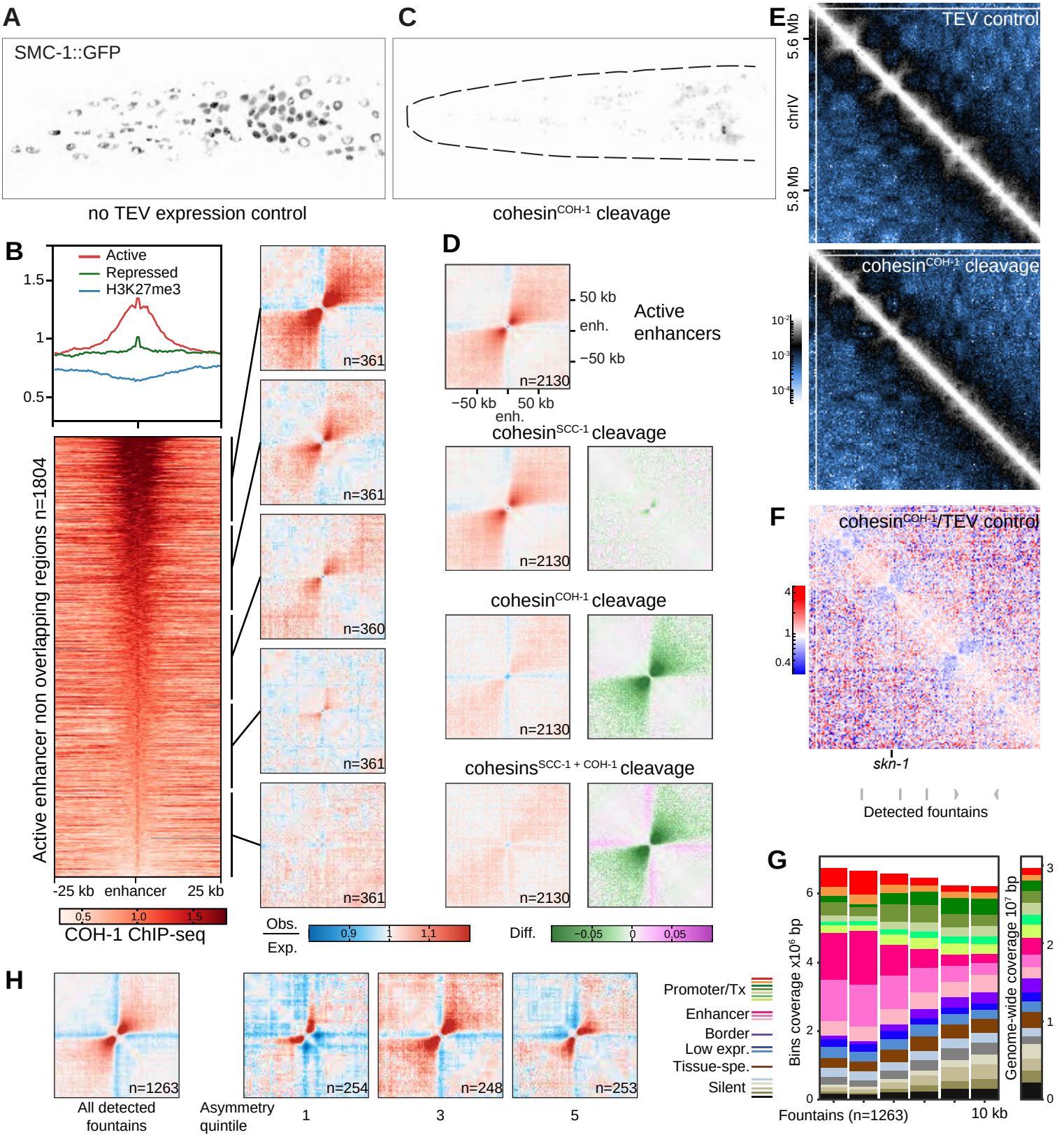

Figure 2. Cohesin^{COH-1} creates fountains at active enhancers.

A. Fluorescence signal in third larval stage no TEV expression control animals expressing SMC-1::GFP. The dark patch in each nucleus corresponds to the nucleolus. **B.** Same as A. in animals after cleavage of COH-1 and SCC-1, which leads to SMC-1::GFP degradation. **C.** (top left) Average COH-1 ChIP-seq profiles in young adult animals at active (red), repressed (green) and H3K27me3 enhancers (blue). (bottom left) Heatmap of COH-1 enrichment on active enhancer regions, sorted by COH-1 ChIP-seq enrichment. (left) Average contact frequency maps centered on enhancers segmented according to COH-1 ChIP-seq abundance. **D.** Cleavage of cohesin^{COH-1} but not cohesin^{SCC-1} leads to disappearance of active enhancer fountains. Average contact frequency maps and difference to control, centered on active enhancers upon cleavage of COH-1 and/or SCC-1. The difference between the different cleavages and TEV control is shown on the right with a green/magenta color scale. **E.** Contact frequency map in TEV control animals (top) and upon cohesin^{COH-1} cleavage (bottom). **F.** Ratio contact frequency map between cohesin^{COH-1} cleavage and TEV control, highlighting the disappearance of the fountains (blue, negative values) and the detected fountains (bottom). **G.** Autosomal chromatin state coverage of detected fountain bins (left) and the adjacent bins, sorted by distance to the detected fountains. Autosome-wide coverage is shown on the right side. **H.** Average contact frequency maps centered on detected fountains for all fountains and for top, middle and bottom asymmetry quintiles of all fountains.

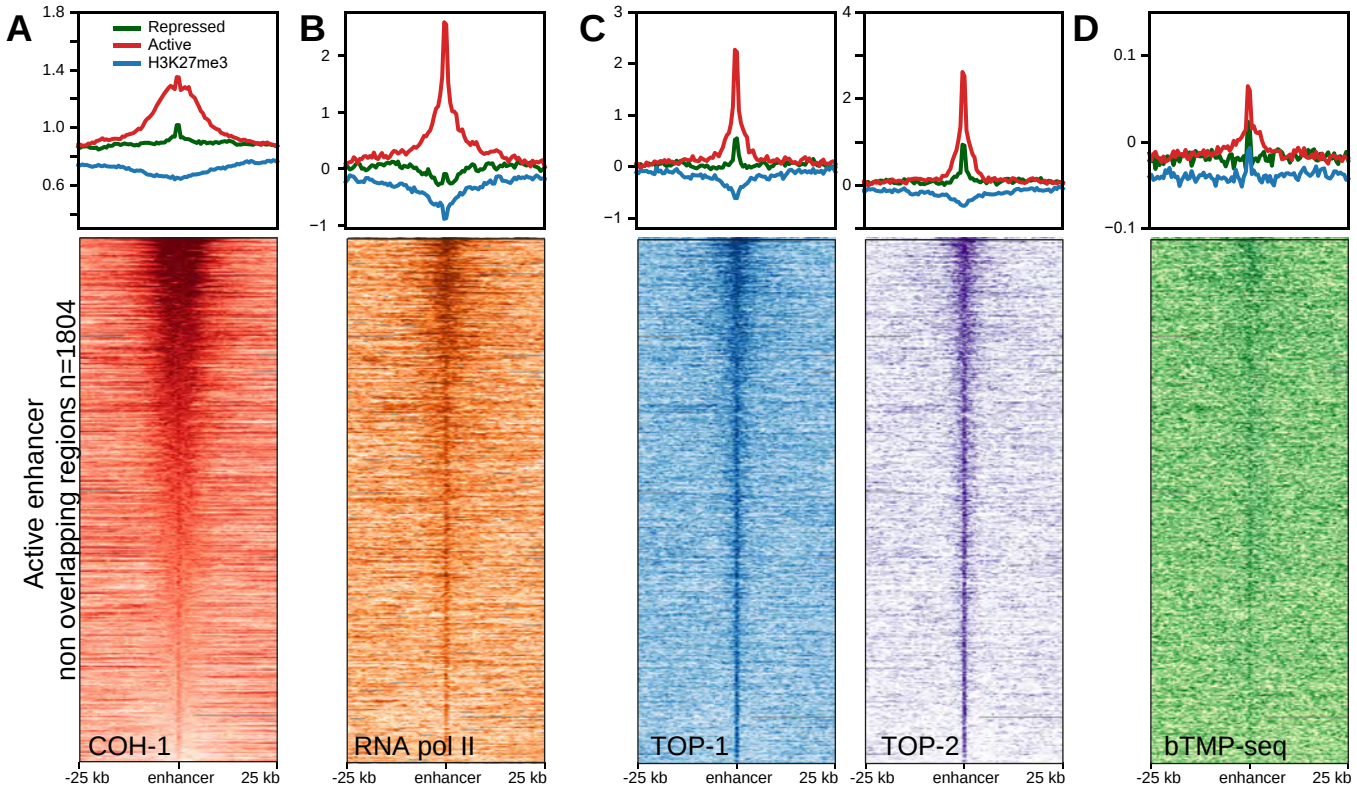
A
B
C
D
Repressed
Active
H3K27me3
Active enhancer
non overlapping regions n=1804
COH-1
RNA pol II
TOP-1
TOP-2
bTMP-seq
-25 kb
enhancer
25 kb

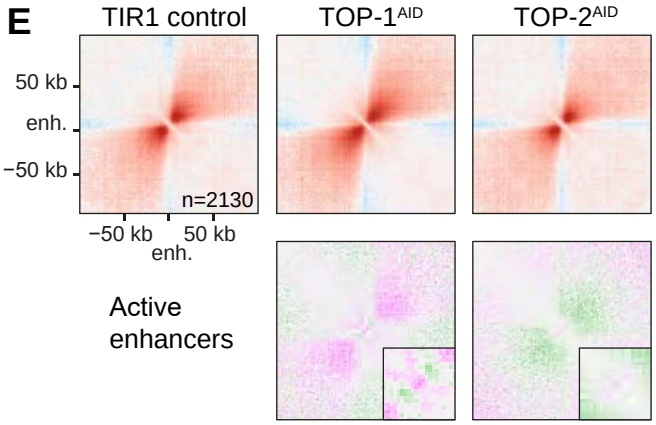
E
TIR1 control
TOP-1AID
TOP-2AID
50 kb
enh.
−50 kb
n=2130
−50 kb
50 kb
enh.
Active
enhancers

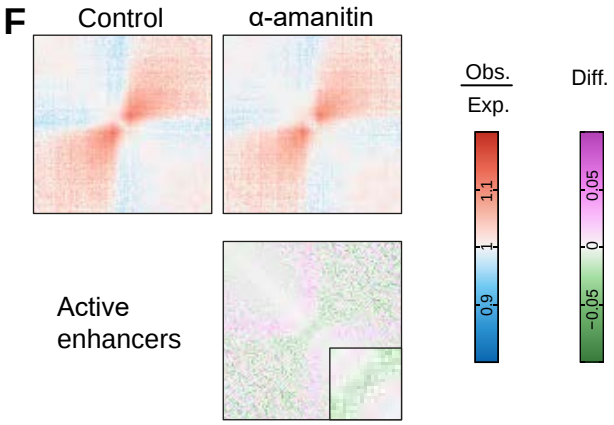
F
Control
α-amanitin
Active
enhancers
Obs.
Exp.
Diff.

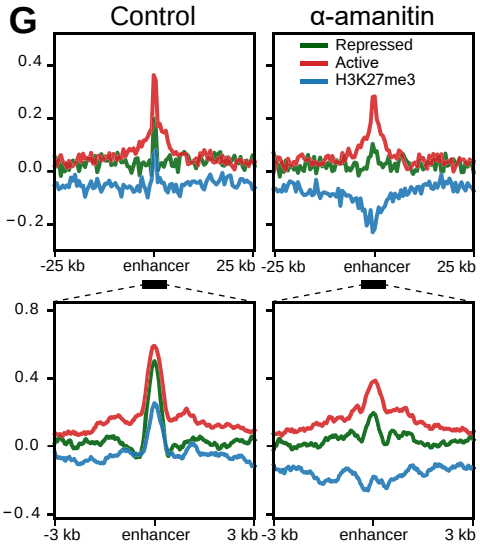
G
Control
α-amanitin
Repressed
Active
H3K27me3
-25 kb
enhancer
25 kb
-3 kb
3 kb

Figure 3. Active enhancers are bound by topoisomerase and enriched for bTMP.
(top) Average ChIP-seq profiles at active, repressed and H3K27me3 enhancers for **A.** COH-1 (young adults), **B.** RNA pol II (L3), **C.** (left) TOP-1 (L3) and (right) TOP-2 (L3). (bottom) Heatmap of **A.** COH-1, **B.** RNA pol II, **C.** (left) TOP-1 and (right) TOP-2 enrichment at active enhancer regions, sorted by COH-1 ChIP-seq enrichment. **D.** (top) Average bTMP-seq profiles in L3 at active, repressed and H3K27me3 enhancers, (bottom) Heatmap of bTMP binding in active enhancer regions, sorted by COH-1 ChIP-seq enrichment. **E.** Depletion of topoisomerases slightly alters fountain strength, especially at the tip. Average contact frequency maps and difference to control, centered on active enhancers. (left) TIR1 control, (right) TOP-1 and TOP-2 AID. (bottom) The difference between the depletion of the topoisomerases and the control, (inset) zoomed in at the fountain tip. **F.** Inhibition of transcription with α-amanitin slightly alters fountain strength, especially at the tip. Average contact frequency maps and difference to control centered on active enhancers. (left) control, (right) α-amanitin inhibited transcription. (bottom) The difference between transcription inhibition and the control, (inset) zoomed in at the fountain tip. **G.** Average bTMP-seq profiles upon transcription inhibition in L3 (top) centered at active, repressed and H3K27me3 enhancers with 25 kb flanking regions (500 bp bin size), (bottom) 6 kb window centered on enhancers (20 bp bin size).

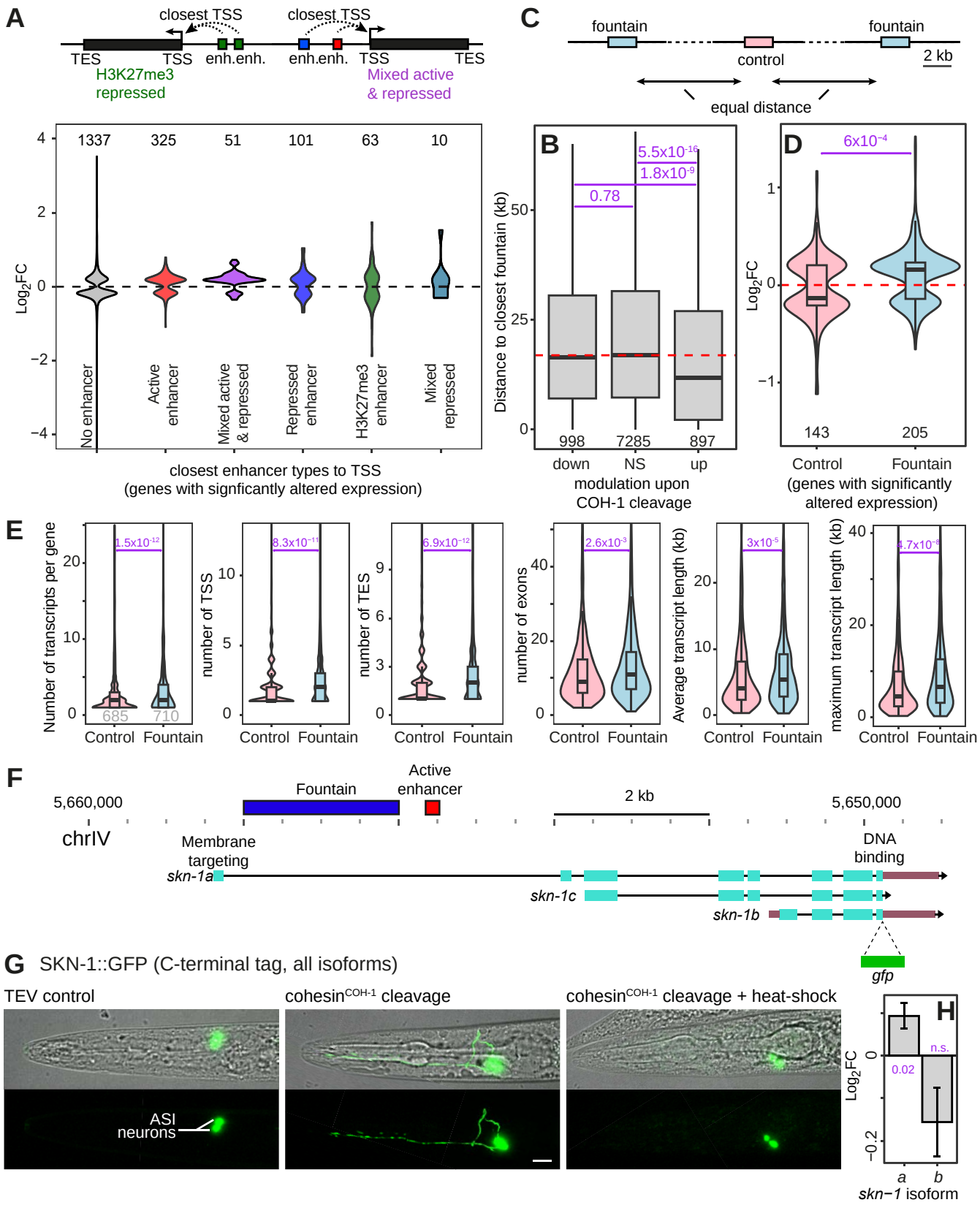
A
closest TSS
closest TSS
TES
TSS
enh.enh.
enh.enh.
TSS
TES
H3K27me3
repressed
Mixed active
& repressed
1337
325
51
101
63
10
Log2FC
No enhancer
Active enhancer
Mixed active & repressed
Repressed enhancer
H3K27me3 enhancer
Mixed repressed
closest enhancer types to TSS
(genes with signficantly altered expression)
C
fountain
control
fountain
2 kb
equal distance
B
5.5x10-16
1.8x10-9
0.78
Distance to closest fountain (kb)
998
7285
897
down
NS
up
modulation upon
COH-1 cleavage
D
6x10-4
Log2FC
143
205
Control
Fountain
(genes with significantly
altered expression)
E
Number of transcripts per gene
1.5x10-12
685
710
Control
Fountain
number of TSS
8.3x10-11
number of TES
6.9x10-12
number of exons
2.6x10-3
Average transcript length (kb)
3x10-5
maximum transcript length (kb)
4.7x10-8
F
5,660,000
chrIV
Fountain
Active enhancer
2 kb
5,650,000
Membrane targeting
DNA binding
skn-1a
skn-1c
skn-1b
gfp
G SKN-1::GFP (C-terminal tag, all isoforms)
TEV control
cohesinCOH-1 cleavage
cohesinCOH-1 cleavage + heat-shock
ASI neurons
H
Log2FC
n.s.
0.02
a
b
skn−1 isoform

Figure 4. Genes upregulated upon COH-1 cleavage have more complex sequence structures.

A. Genes were grouped according to the types of L3 stage enhancers from Daugherty *et al.* (2017) that their TSS was closest to. The log2 fold change of genes that were significantly up or down regulated (adjP<0.05) upon cleavage of COH-1^{cs} are plotted according to enhancer type. **B.** Boxplot of the distance of genes from the nearest fountain bin. Genes were grouped by their change in expression upon COH-1 cleavage: up and down regulated or not changing significantly (NS). The dashed red line indicates the median distance to the nearest fountain bin of NS genes. In B,D & E, the number of genes in each group is indicated at the bottom of the plot, and adjusted p-values from Wilcoxon rank sum tests are shown in purple **C.** Schematic representation of regions used in panels D-E. 2kb fountain bins were compared with control bins of the same size located at the midpoint between neighboring fountains. **D.** Log2 fold change upon COH-1^{cs} cleavage of significantly changing genes (adjP<0.05) that overlap control bins (143 genes) and fountain bins (205 genes). **E.** Comparison of features of genes that overlap with control and fountain bins. **F.** Structure of the *skn-1* genomic region, highlighting the three canonical *skn-1* isoforms *a* to *c*, the location of the GFP transgene insertion used in G, the characterized active enhancer and the detected fountain location. **G.** Expression of *skn-1* in the head of control animals, upon COH-1 cleavage or upon COH-1 cleavage and heat stress 30' prior imaging. Scale bar = 10 µm. The two ASI head neurons are indicated on the left-most panel. **H.** Transcript level differential expression of skn-1 isoforms upon coh-1 cleavage. Adjusted p values from Wald test are shown next to the bars (n.s. is not significant).

Isiaka et al., Figure 5

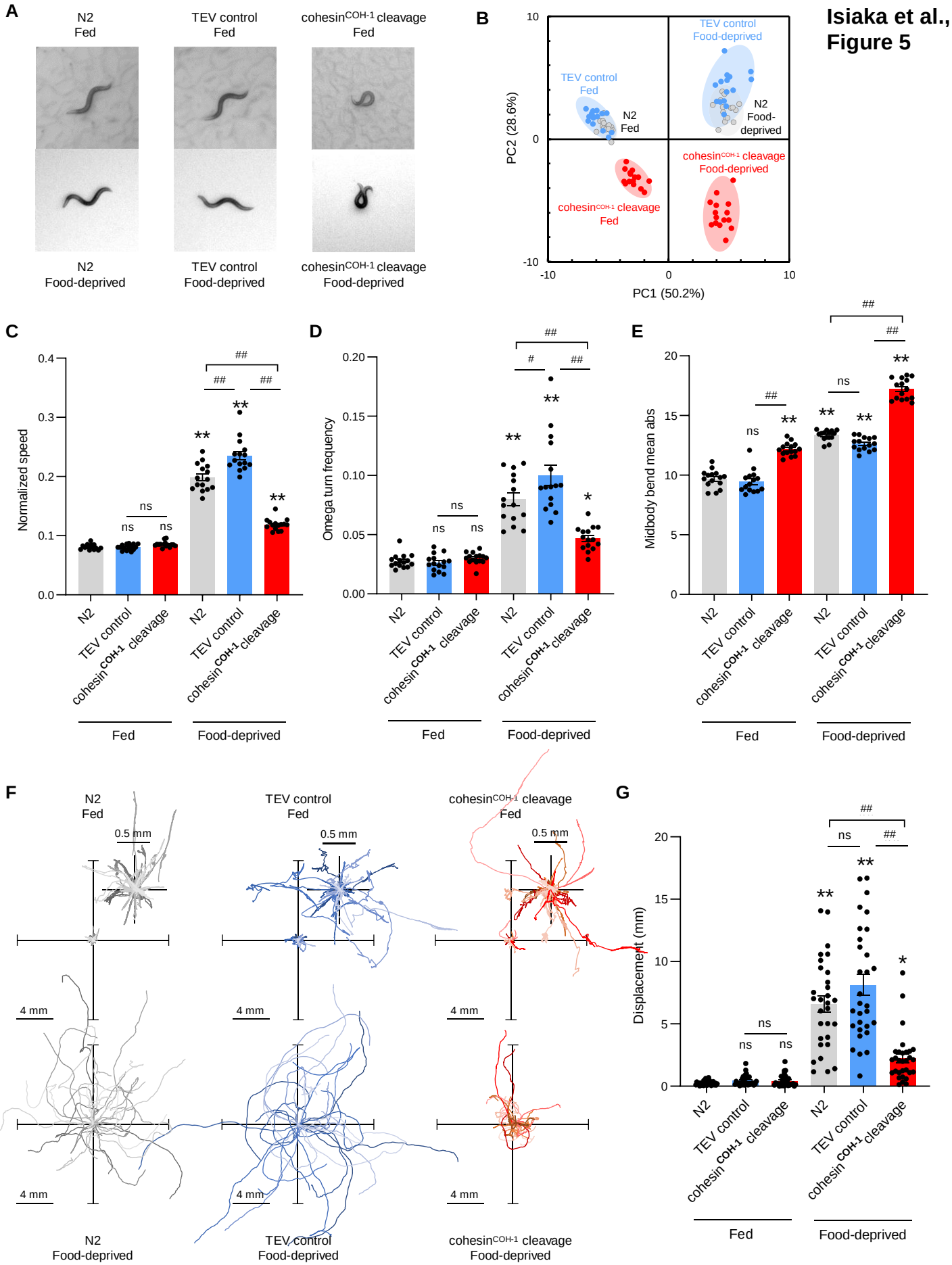

Figure 5. COH-1 cleavage affects the nervous system function, producing multiple postural and locomotion alterations

A. Representative pictures of young adult *C. elegans* either dwelling on food (Fed) or foraging off-food 6 hours after food deprivation (Food-deprived), illustrating postural differences between the indicated genotypes. **B**. Multidimensional behavioral states of animals presented as projections over the two main principal components (PC1 and PC2) from a single principal component analysis (PCA) over 47 postural and motion parameters, and over all the conditions. The proportion of variance explained by each PC is indicated in the axis labels. Upper left and upper right quadrants (respectively) correspond to the normal dwelling and food search behavioral states adopted by wild type or TEV control worms. The lower left and right quadrants correspond to markedly altered behavioral states caused by COH-1 cleavage. Averages positions of individual replicates as data marks, 95% CI as colored ellipses. Each replicate is a separate worm population with ≥40 animals. **C-E**. Selected behavioral parameters reported as average ± s.e.m. of n = 15 independent replicates. Each replicate value (data points) corresponds to the average value of a separate worm population with ≥40 animals. Additional behavioral alterations are presented in Supplementary Fig. S5. **F**. One-minute worm trajectories (35 for each condition) plotted from a single starting (0,0) coordinate. Enlarged representations for fed worms in dwelling state (insets). **G**. Dispersal quantification. Average ± s.e.m. and individual data points for animal displacement (corresponding to how far animals moved from their starting point). n=30 animals. **C**, **D**, **E**, **G**. *, p<.05 and **, p<.01 versus N2 Fed condition, # p<.05 and ##, p<.01 versus the indicated control by Bonferroni posthoc tests.

Supplementary figures and legends

Isiaka et al., Figure S1

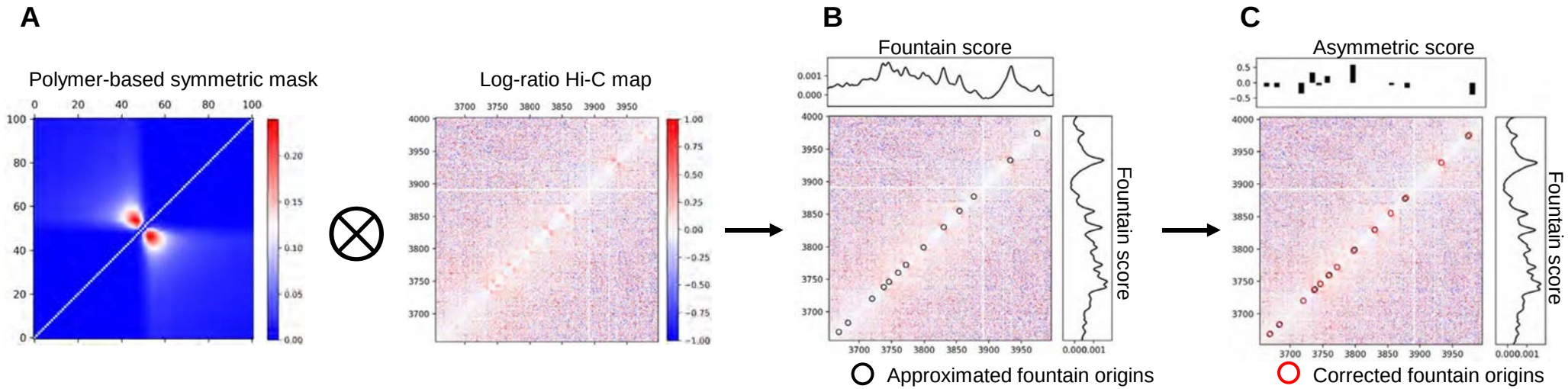

Supplementary Figure 1

Inferring fountain positions and asymmetries

Pipeline for the detection of fountain origins. **A.** A polymer-model-based mask of a symmetric fountain is convoluted along the diagonal of the log-ratio matrix (WT divided by cohesin-depleted) to compute a local fountain score. **B.** Maxima of the profile of fountain score along the genome with significant prominence are assigned as approximated fountain origins. **C.** Correction for asymmetry in fountain shapes is performed to localizeprecisely the position of fountain origin and their asymmetries (<0: left-handed fountain, >0: right-handed fountain).

Isiaka et al., Figure S2

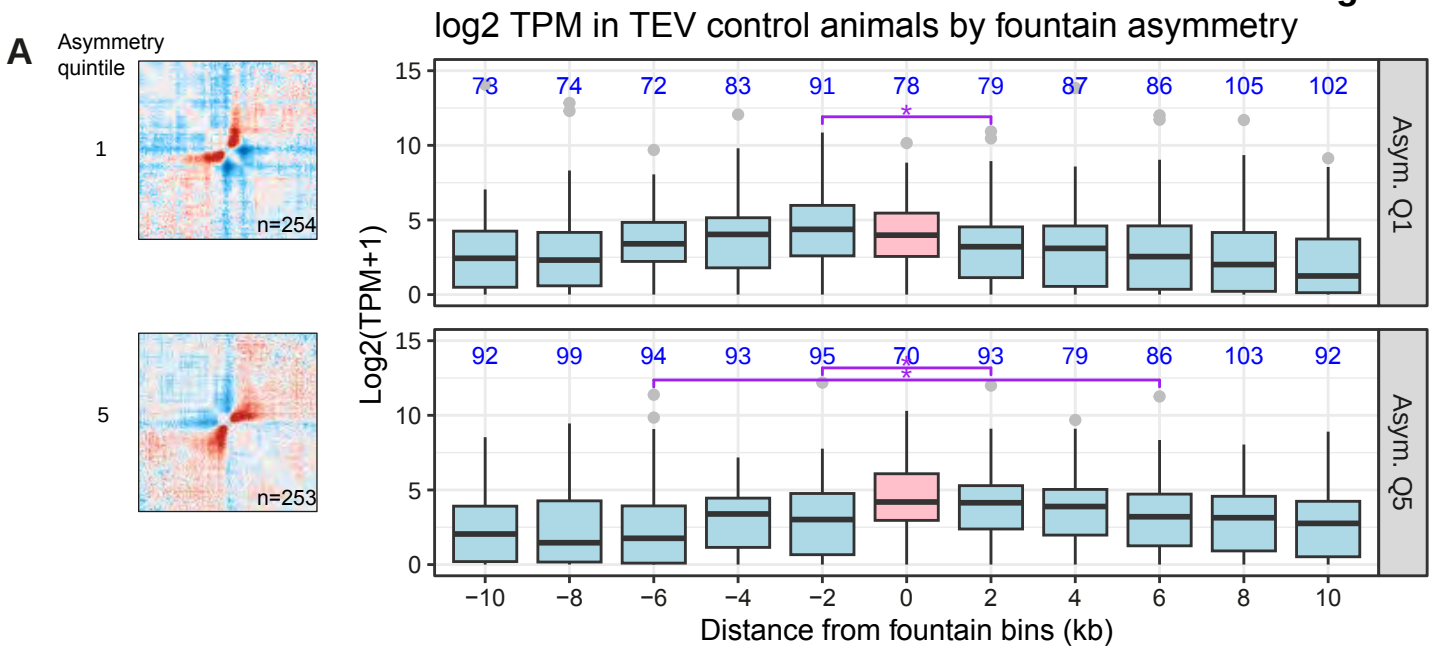

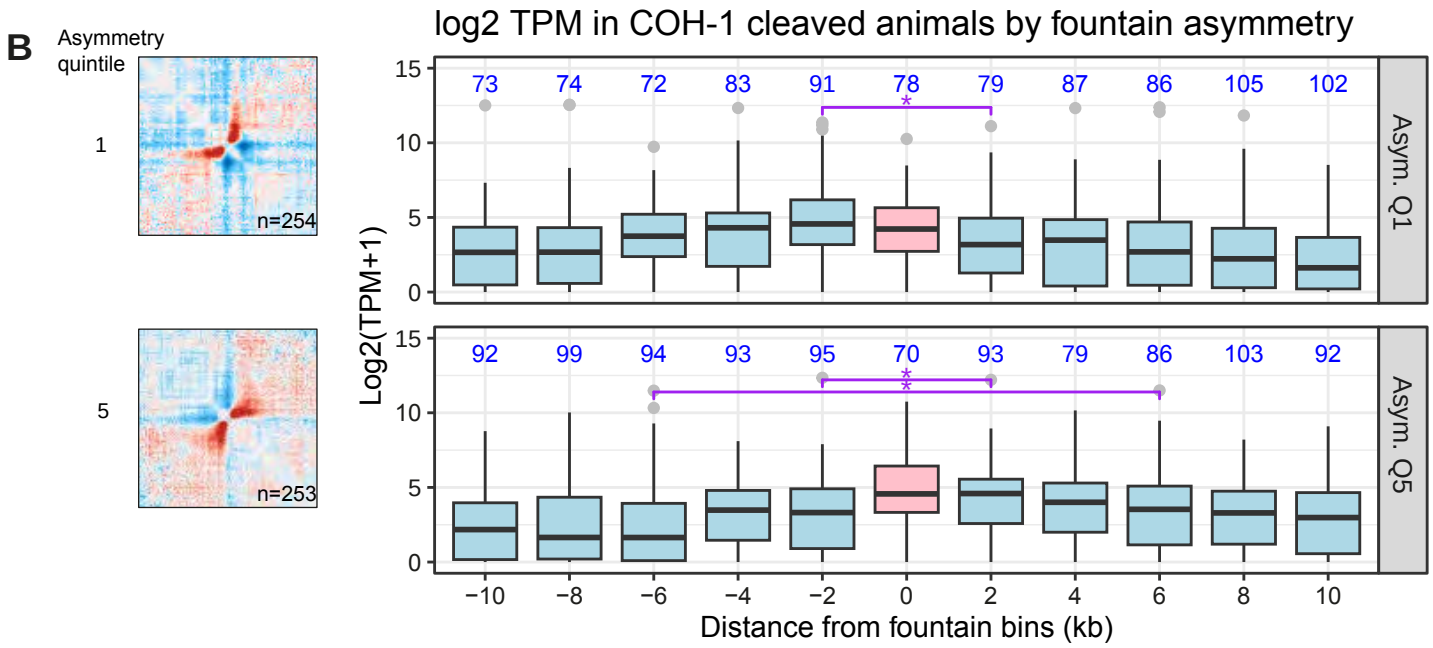

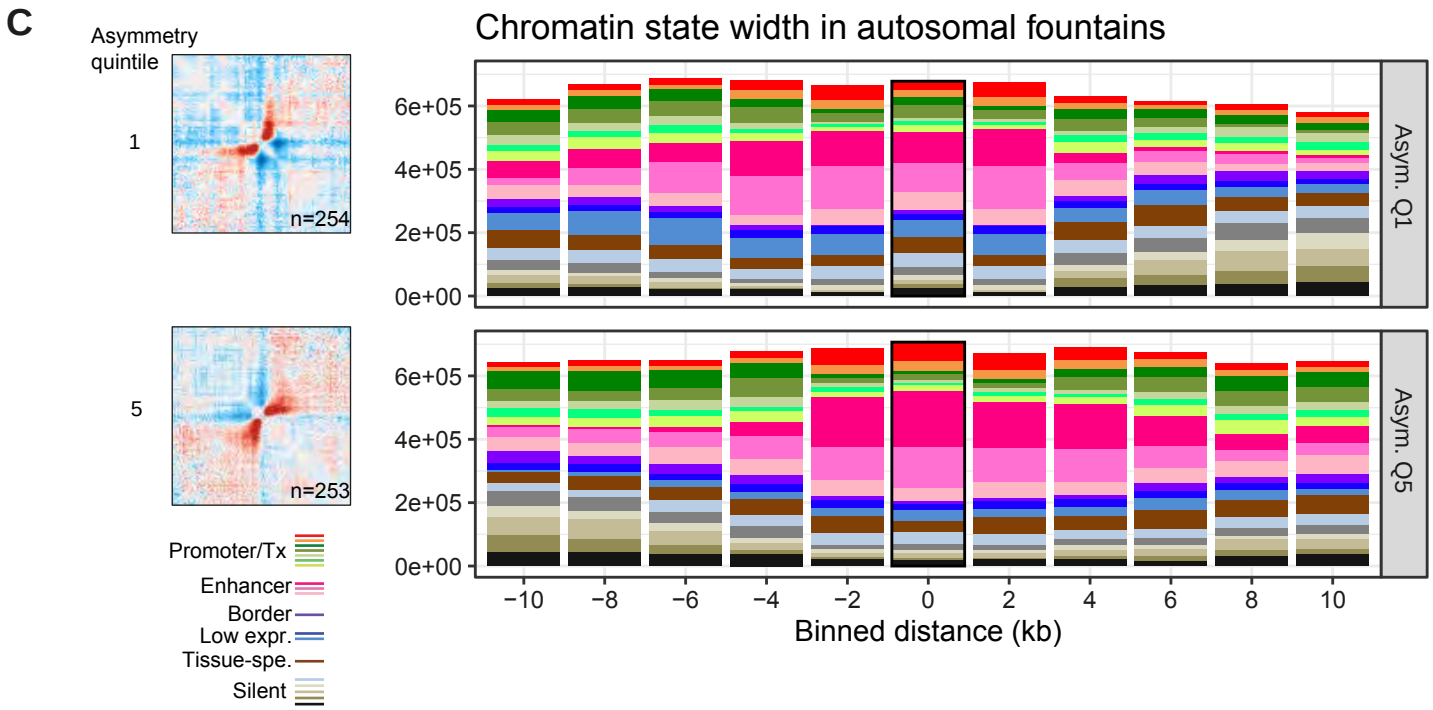

Supplementary Figure 2

Fountain asymmetry is associated with asymmetry in absolute expression levels

Fountain asymmetry scores were divided into five equally sized bins (quintiles). 2kb bins overlapping the fountains from the highest and lowest quintiles, and up to 10kb upstream and downstream, were used to quantify transcript abundance for genes that overlap them. **A.** Left panel: pileup of HiC regions around asymmetric fountains from the first and fifth quintiles. Right panel: Boxplot of gene expression (TPM) in TEV-only control samples of genes whose TSSs overlap the respective 2kb bins around fountains. **B.** Left panel as in A. Right panel: Boxplot of gene expression (TPM) in COH-1 cleavage samples of genes whose TSSs overlap the respective 2kb bins around fountains. In both A and B the purple line indicates a significant difference in expression between bins upstream and downstream of the fountains. The number of genes in each bin are indicated in blue. **C.** Left panel as in A. Right panel: Total width in bp of each chromatin state found in 2kb bins surrounding fountains from the first and fifth asymmetry quintile.

A

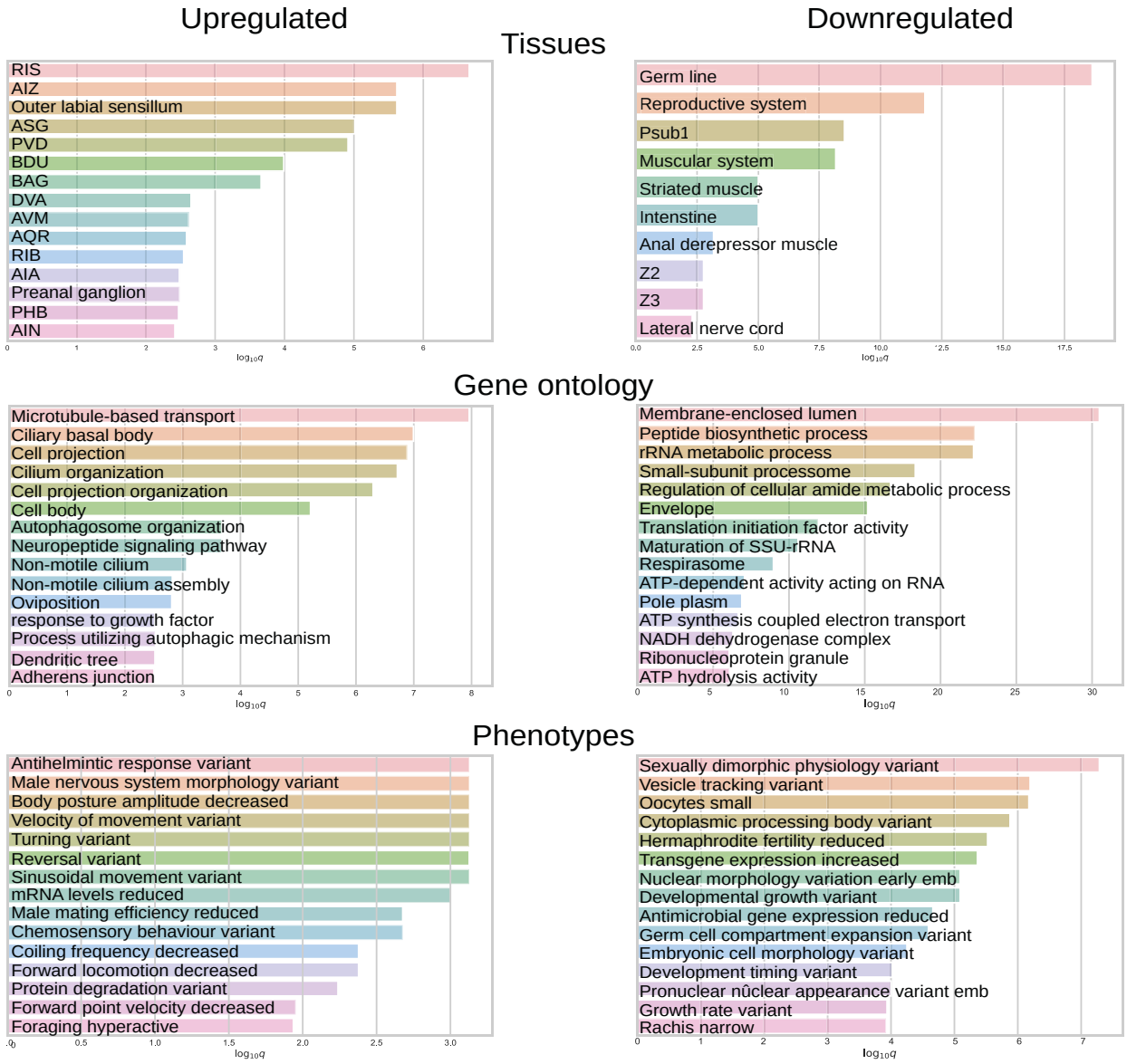
Upregulated
Downregulated
Tissues
RIS
AIZ
Outer labial sensillum
ASG
PVD
BDU
BAG
DVA
AVM
AQR
RIB
AIA
Preanal ganglion
PHB
AIN
Germ line
Reproductive system
Psub1
Muscular system
Striated muscle
Intenstine
Anal derepressor muscle
Z2
Z3
Lateral nerve cord
Gene ontology
Microtubule-based transport
Ciliary basal body
Cell projection
Cilium organization
Cell projection organization
Cell body
Autophagosome organization
Neuropeptide signaling pathway
Non-motile cilium
Non-motile cilium assembly
Oviposition
response to growth factor
Process utilizing autophagic mechanism
Dendritic tree
Adherens junction
Membrane-enclosed lumen
Peptide biosynthetic process
rRNA metabolic process
Small-subunit processome
Regulation of cellular amide metabolic process
Envelope
Translation initiation factor activity
Maturation of SSU-rRNA
Respirasome
ATP-dependent activity acting on RNA
Pole plasm
ATP synthesis coupled electron transport
NADH dehydrogenase complex
Ribonucleoprotein granule
ATP hydrolysis activity
Phenotypes
Antihelmintic response variant
Male nervous system morphology variant
Body posture amplitude decreased
Velocity of movement variant
Turning variant
Reversal variant
Sinusoidal movement variant
mRNA levels reduced
Male mating efficiency reduced
Chemosensory behaviour variant
Coiling frequency decreased
Forward locomotion decreased
Protein degradation variant
Forward point velocity decreased
Foraging hyperactive
Sexually dimorphic physiology variant
Vesicle tracking variant
Oocytes small
Cytoplasmic processing body variant
Hermaphrodite fertility reduced
Transgene expression increased
Nuclear morphology variation early emb
Developmental growth variant
Antimicrobial gene expression reduced
Germ cell compartment expansion variant
Embryonic cell morphology variant
Development timing variant
Pronuclear nûclear appearance variant emb
Growth rate variant
Rachis narrow
log10q

B

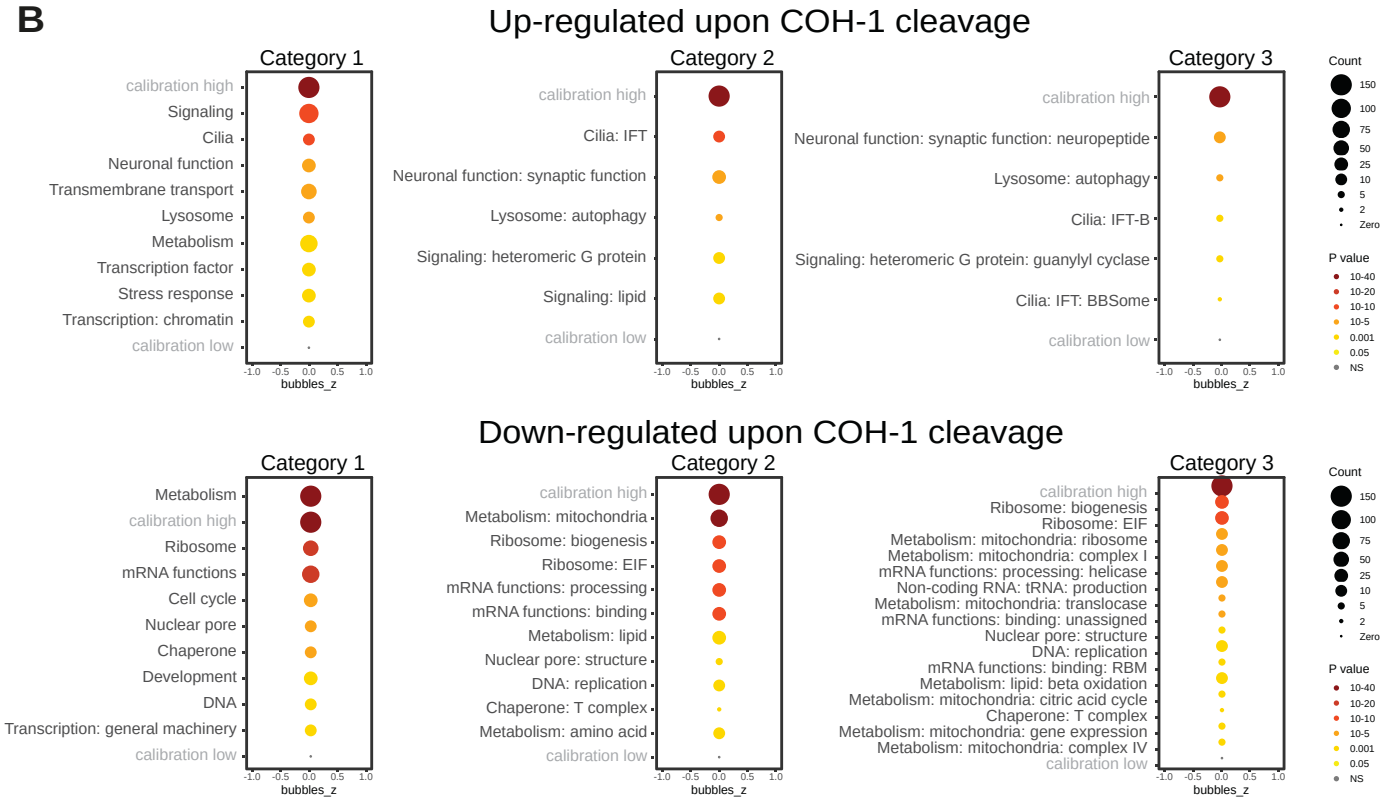
Up-regulated upon COH-1 cleavage
Category 1
calibration high
Signaling
Cilia
Neuronal function
Transmembrane transport
Lysosome
Metabolism
Transcription factor
Stress response
Transcription: chromatin
calibration low
Category 2
calibration high
Cilia: IFT
Neuronal function: synaptic function
Lysosome: autophagy
Signaling: heteromeric G protein
Signaling: lipid
calibration low
Category 3
calibration high
Neuronal function: synaptic function: neuropeptide
Lysosome: autophagy
Cilia: IFT-B
Signaling: heteromeric G protein: guanylyl cyclase
Cilia: IFT: BBSome
calibration low
bubbles_z
Count
150
100
75
50
25
10
5
2
Zero
P value
10-40
10-20
10-10
10-5
0.001
0.05
NS
Down-regulated upon COH-1 cleavage
Category 1
Metabolism
calibration high
Ribosome
mRNA functions
Cell cycle
Nuclear pore
Chaperone
Development
DNA
Transcription: general machinery
calibration low
Category 2
calibration high
Metabolism: mitochondria
Ribosome: biogenesis
Ribosome: EIF
mRNA functions: processing
mRNA functions: binding
Metabolism: lipid
Nuclear pore: structure
DNA: replication
Chaperone: T complex
Metabolism: amino acid
calibration low
Category 3
calibration high
Ribosome: biogenesis
Ribosome: EIF
Metabolism: mitochondria: ribosome
Metabolism: mitochondria: complex I
mRNA functions: processing: helicase
Non-coding RNA: tRNA: production
Metabolism: mitochondria: translocase
mRNA functions: binding: unassigned
Nuclear pore: structure
DNA: replication
mRNA functions: binding: RBM
Metabolism: lipid: beta oxidation
Metabolism: mitochondria: citric acid cycle
Chaperone: T complex
Metabolism: mitochondria: gene expression
Metabolism: mitochondria: complex IV
calibration low

Supplementary Figure 3

GO term, tissue and phenotype enrichment for genes changing upon COH-1 cleavage.

A. Tissue Enrichment Analysis for genes significantly up and down regulated upon COH-1^{cs} cleavage (adjP<0.05), using tissues, Gene Ontology and Phenotypes annotations (Angeles-Albores et al., 2016). **B.** WormCat enrichment analysis for genes significantly up and down regulated upon COH-1^{cs} cleavage (adjP<0.05; (Holdorf et al., 2020).

Isiaka et al.,
Figure S4

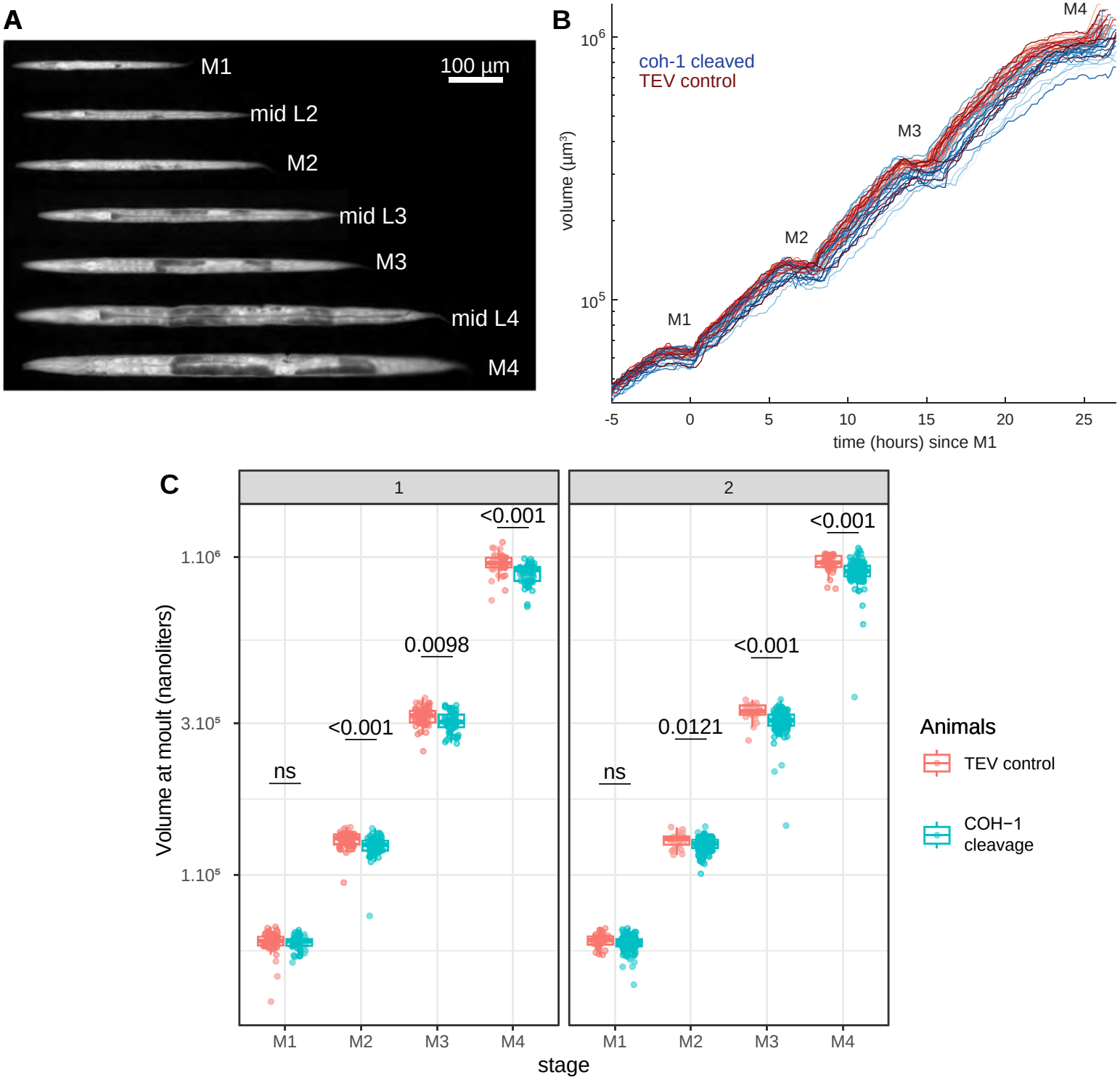

Supplementary Figure 4

Growth analysis of animals upon TEV only expression or COH-1 cleavage

A. An individual animal imaged in a micro chamber at indicated developmental milestones. Contrast was adjusted for each time point individually and the animal straightened computationally. Scale bar: 100 µm. **B.** Example growth curves for 10 control animals and 10 animals upon COH-1 cleavage, synchronized on the first molt. Molts are marked by M. **C.** Body volume at molts for two independent experiments in control animals and upon COH-1 cleavage, n= 57;60 (first experiment), 29;122 (second experiment). Box represents 1st quartile, median and the 3rd quartile of the data (bottom to top), with individual animals marked as dots. Values above samples are Wilcoxon rank sum test p-values.

Isiaka et al., Figure S5

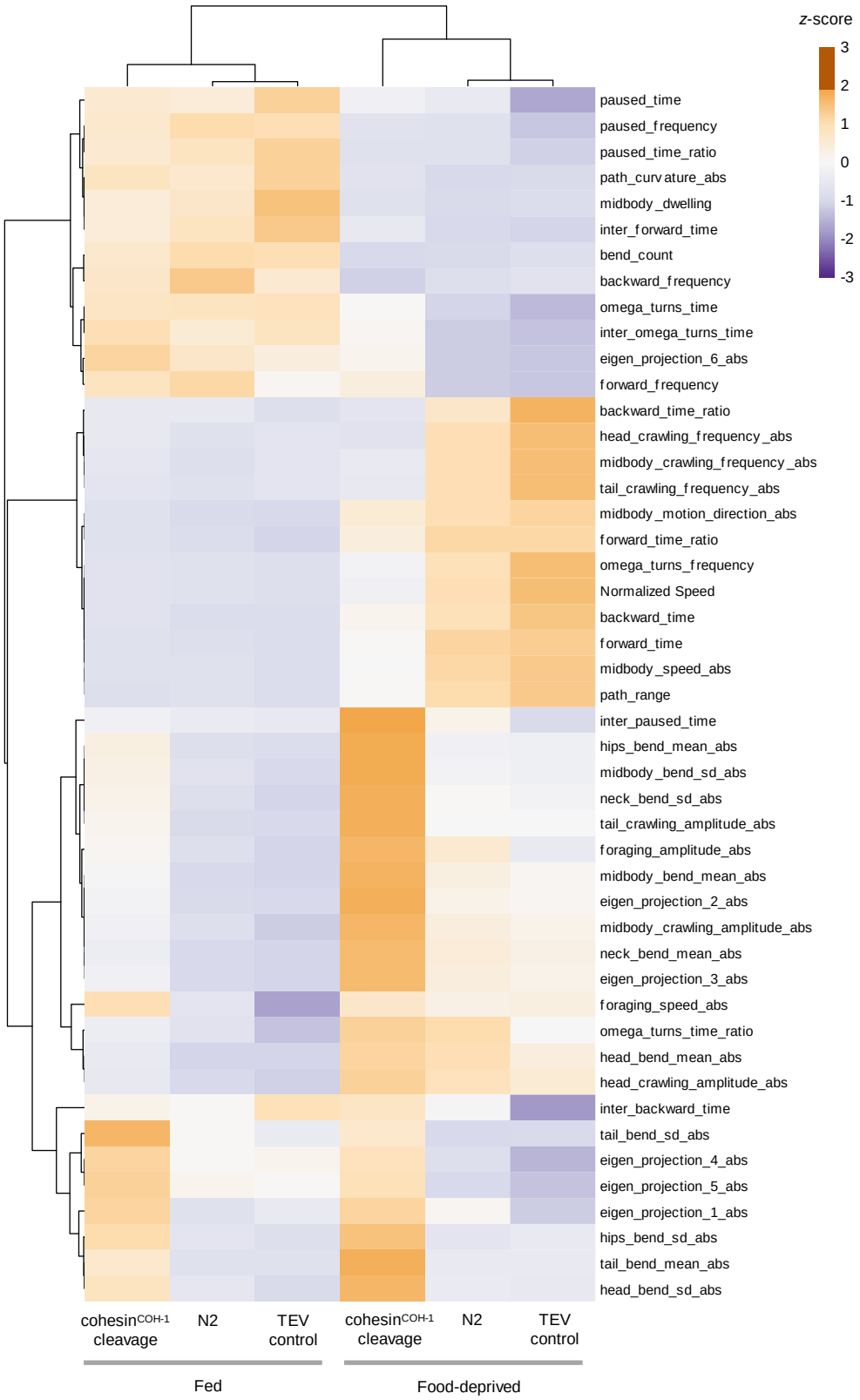

Supplementary Figure 5

COH-1 cleavage produces pleiotropic effects on worm posture and locomotion

Heat-map of behavioral parameters (as z-scores) across the indicated conditions (same treatment as in Fig. 5) and hierarchical clustering based on Euclidean distances (trees). Each data point represents the average value for 3-min recordings on n = 15 independent replicates (each scoring ≥40 worms).

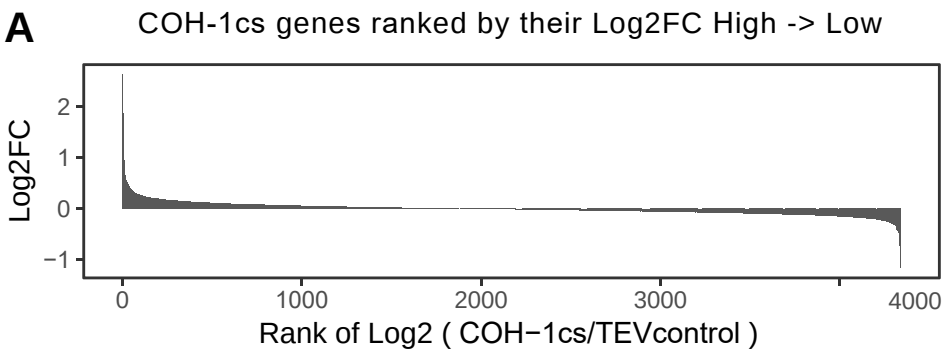

Test ranking of worm orthologs of Cornelia de Lange Syndrome genes
(up and down gene sets, CdLS Neu+ vs control Neu+, Weiss *et al.* 2021)

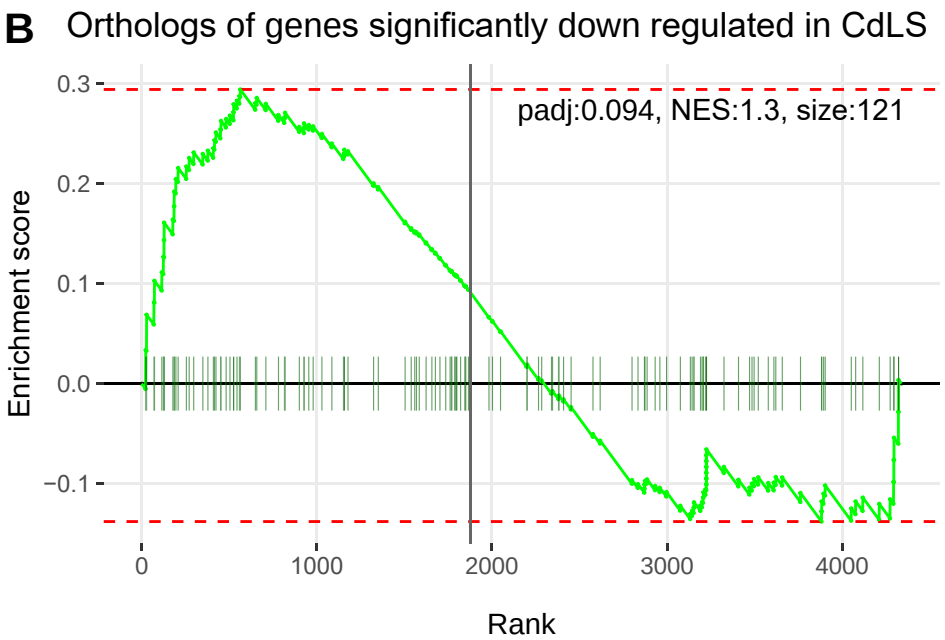

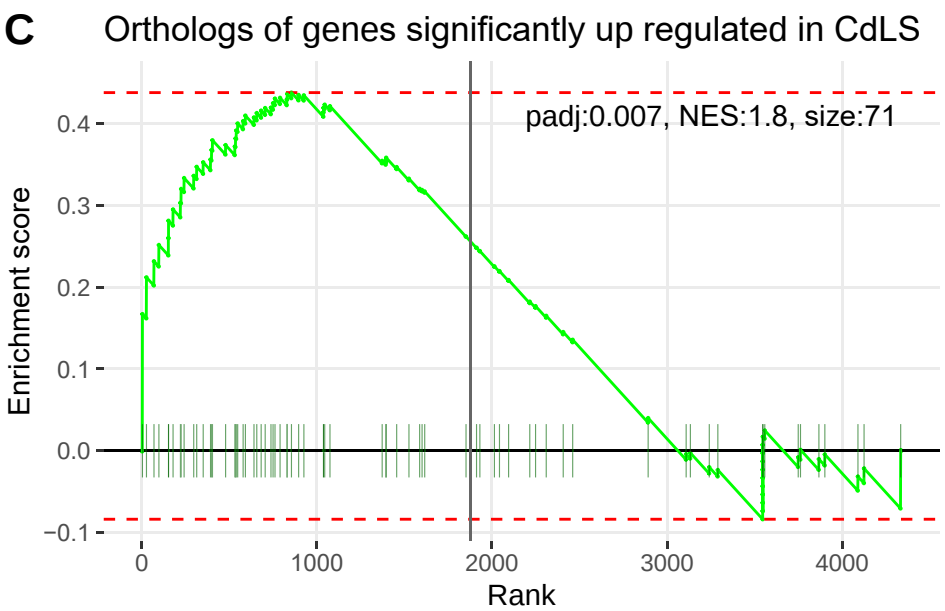

Supplementary Figure 6

Gene set enrichment analysis (GSEA) of Cornelia de Lange syndrome genes among their nematode orthologs ranked by their log2FC upon COH-1 cleavage.

A. Schematic of GSEA procedure: Genes were ranked in descending order by their log2 fold change upon COH-1 cleavage. The ranks of *C. elegans* orthologs of genes significantly changing in Cornelia de Lange Syndrome (CdLS) patient neurons vs control neurons (Weiss et al 2021) were tested for enrichment. **B.** Enrichment of nematode orthologs of genes significantly down regulated in CdLS patient neurons. **C.** Enrichment of nematode orthologs of genes significantly up regulated in CdLS patient neurons. The adjusted p value (padj), normalized enrichment score (NES) and the size of the gene set is shown in each panel on the top right corner. Green ticks indicate the position of the orthologs of CdLS genes among the nematode genes ranked by their log2FC upon COH-1 cleavage. The light green line indicates the enrichment score: a running sum of the degree to which the CdLS genes are enriched at the beginning of the COH-1 cleavage ranked list (positive values) vs the end of the list (negative values).

Methods

General worm growth and collection

A large unsynchronized worm population of the genotype of interest was grown on four 140 mm peptone-rich plates for about three days to get gravid adults. The worms were bleached, and the eggs hatched overnight in the M9 buffer without food. The synchronized L1s were plated on four 140 mm NGM plates (80,000 – 100,000 worms per plate) and left to grow at 22 ℃ for 24 hours. For specific conditions requiring TEV expression, synchronized L1 animals were left on NGM food for 3 hours, before heat-shocking them at 34°C for 30 minutes. After 19 hours, the L3s were washed from the plates using M9 and did a couple of washes to remove bacteria before proceeding with downstream experiments. For the genomic DNA experiments, the L3s were resuspended in 20 ml of ice-cold M9 and 20 ml of ice-cold 60 % sucrose, shaken vigorously, and gently layered 4 ml of ice-cold M9 on top. 30 ml of the supernatant (on top of the sucrose), now containing floating worms, is aspirated and distributed into 50 ml falcon tubes that were subsequently filled to 50 ml with ice-cold M9. Spun at 1000 rpm for 1 minute at room temperature, discarded the liquid, and washed the worms with ice-cold M9 and once with room-temperature M9. The worms were left at room temperature for 25 minutes for the remaining bacteria in the worms' gut to get digested, washed once with M9, and removed liquid before proceeding to DNA isolation.

RNA-seq

RNA sequencing libraries were made by Novogene before sequencing using Illumina NovaSeq (paired-end (PE), 150 bp read length). Reads were aligned to the WS285 transcriptome with Salmon (v.1.9.0) in quant mode with the flags --validateMappings --seqBias --gcBias. Counts per gene were compared with DESeq2 (v1.36.0). GO term enrichment was performed using command line versions of the Wormbase TEA tool (Angeles-Albores et al., 2016) and WormCat (Holdorf et al., 2020). The COH-1^{cs} RNAseq data was taken from (Das et al., 2022) but reanalysed on its own comparing just the COH-1^{cs} (PMW828) strain to the TEV-only control strain (PMW366), aligned to the WS285 transcriptome and pre-filtered before DESeq2 analysis to only include samples with at least 10 reads in half the samples. The different pipeline yielded slightly different results tables, but correlation of the shrunken log2 fold change was 0.97. Of a total 9180 genes left after filtering out genes that oscillate during development (Latorre et al., 2015; Meeuse et al., 2020), 895 were significantly up regulated and 993 down regulated (adjP<0.05), but as noted previously (Das et al., 2022), most of the log2 fold changes were extremely small, with only 98 genes having a LFC > 0.5 and 52 genes with a LFC < -0.5. Transcript level quantification was carried out by mapping reads to transcripts using Salmon as described

above, but adding 100 bootstrap samples. The counts were converted to hd5 format with Wasabi (version 1.0.1) and differential expression was carried out with Sleuth (version 0.30.1), filtering out low count transcripts with the default basic_filter, and also removing transcripts from oscillating and non-protein-coding genes by their ids.

Nuclei Isolation

400,000 L3s worms were washed with cold nuclear isolation buffer (NIB) (250 mM sucrose, 10 mM Tris-HCl (pH 7.9), 10 mM $MgCl_2$, 1 mM EGTA, 0.25 % NP-40, 1 mM DTT, and protease inhibitors). Spun for 1 minute in a microcentrifuge, discarded the supernatant, and then snap-freeze the reaction tube in liquid nitrogen. The frozen worm pellet was squeezed into a pre-chilled mortar, placed in a ceramic bowl, put the pestle in it, and hit five times with a hammer. Removed the pestle and ground it into powder form with an electric drill. The powder was scraped from the mortar into a new tube. An equal volume of NIB was added to the powder, and the fully thawed mixture was transferred into a Kontes™ 2ml glass dounce on ice and centrifuged at 4℃. Dounced the ground-up worms ten times with the “loose” pestle, then ten times with the “tight” pestle, after which it was transferred to a 1.5 ml Eppendorf tube and centrifuged for five minutes at 100 rcf in a microcentrifuge. The supernatant was transferred to a new Eppendorf tube, making sure not to take up any worm debris. Added an equal volume of NIB again and repeated the douncing and spinning four more times till all nuclei were collected. The nuclei are then counted using a hemocytometer and fluorescent microscope.

bTMP-Seq

bTMP was synthesized as described (Naughton et al., 2013) and supplied by Nick Gilbert’s research group. Washed nuclei with wash buffer (WB) (10 mM Tris (pH 7.4), 10 mM NaCl, 3 mM $MgCl_2$, and 0.1 mM EDTA) to remove leftover NIB. Centrifuged for five minutes at 3000 rpm at 4 ℃ in a microcentrifuge and discarded the supernatant. Making sure to work with 10 million nuclei per 200 µl volume wash buffer, added 4 µl of 30 mg/ml stock solution of bTMP (i.e., 600 µg/ml final concentration) to the sample. The reaction mixture was incubated in the dark at room temperature for 30 minutes in an Eppendorf tube on a rotator. Transferred the sample into a 96-well plate to increase the surface area and crosslinked for 10 minutes (8000 energy). Transferred nuclei to a 1.5 ml Eppendorf tube and spun down at 3000 rpm at 4 ℃ in a microcentrifuge for five minutes. The supernatant was discarded, and the volume was made up to 600 µl with WB and incubated with 200 µg/ml proteinase K (12 µl of 20 mg/ml stock) at 55 ℃ for 16 hours (overnight). DNA was purified by phenol:chloroform extraction and isopropanol precipitation as follows: Added an equal volume of

phenol:chloroform to the sample and transferred it to a 2 ml PLG tube and mixed thoroughly by inversion for 1 minute. Spun in a microcentrifuge at room temperature to separate the phases at maximum speed and transferred the top aqueous phase to a new 1.5 ml Eppendorf tube. The phenol:chloroform extraction was repeated once. Added 0.6 volumes of 2-Propanol, mixed by inverting the tube once, and spun at maximum speed for 30 minutes at room temperature in a microcentrifuge. All the 2-Propanol was discarded by decanting, washed the pellet twice with freshly prepared 70 % ethanol, and spun for 1 minute at room temperature at maximum speed between the washes. After the last wash, removed all traces of ethanol by inverting the tube and allowed to dry for approximately 10 minutes. DNA was resuspended in 41 µl 1x TE buffer (10 mM Tris (pH7.4), 1 mM EDTA) and quantified by QuantiFluor® dsDNA System (Promega). The DNA (1-2 µg DNA / 100 µl volume) was fragmented into approximately 400 bp fragments using the Bioruptor® sonication system (diagenode) at 30 seconds ON and 90 seconds OFF at low power setting for 12 minutes. For the immunoprecipitation (IP), 20 ng of the DNA sample was collected as input and stored at -20 ℃. The rest of the sample was made up to 1 ml with 1x TE buffer. In a 1.5 ml Eppendorf, 1 ml 1x TE buffer and 50 µl avidin conjugated to magnetic beads (Dynabeads™ MyOne™ Streptavidin C1) were added. The mix was rotated at room temperature for 5 minutes and separated from the beads from the wash on a magnetic stand, after which the clear liquid was discarded; this wash step was repeated twice with 1x TE buffer. Added the 1 ml DNA sample to the washed beads and rotated overnight at 4 ℃. Placed the reaction tube on a magnetic stand and removed and discarded the clear liquid. Washed the DNA-bound beads with 1 ml of TSE I (20 mM Tris-HCl pH 8.1, 2 mM EDTA, 150 mM NaCl, 1 % Triton X-100, and 0.1 % SDS) and mixed by rotating at room temperature for 5 minutes, separated the beads from the wash on a magnetic stand after which the clear liquid was discarded. Subsequent washes were done with TSE II (20 mM Tris-HCl pH 8.1, 2 mM EDTA, 500 mM NaCl, 1 % Triton X-100, and 0.1 % SDS), TSE III (20 mM Tris, pH 8.1, 0.25 M LiCl, 1 mM EDTA, 1 % NP-40 and 1 % deoxycholate (DOC)) and 1x TE buffer as done for TSE I. The IP DNA was eluted by adding a 50 µl elution mix (10 mM EDTA and 95 % formamide) and heated at 95 ℃ for 10 minutes, vortexing the sample every 2 to 3 minutes. Placed the reaction tube on a magnetic stand and transferred the clear elute to a new 1.5 Eppendorf tube. Added 150 µl Milli-Q water to make up to 200 µl and purified the DNA according to the SPRIselect User Guide for SPRI-based size selection. 20 µl of Milli-Q water preheated to 70 ℃ was used for the final DNA elution, and transferred the elute to a new tube and quantified the DNA by Qubit. The Illumina library was then made according to the NEBNext® Ultra™ II DNA library Prep kit for illumina® instruction manual and followed the standard protocol. The libraries were then sequenced at the Next Generation Sequencing (NGS) platform of the

University of Bern on Illumina NovaSeq 6000 (single end (SE) 50 bp read length). The sequence data can be found in the supplementary table.

bTMP-seq data analysis

The data generated were preprocessed as follows: Adapter was trimmed using Trim Galore! Version 0.6.6, after which the reads were aligned to the *C. elegans* reference genome version ce11 using Burrows-Wheeler Aligner (BWA) version 0.7.17. The aligned reads were then sorted based on their genomic coordinates using Samtools version 1.8. Sequencing duplicate reads were removed using Picard version 2.21.8, after which blacklisted genes regions and multi-mapping reads were removed using Samtools. For each control and treatment replicates per experiment, the reads were subsampled to the lowest number of reads (>= 5 million reads), after which the read length was elongated to fragment length by extending reads to 200 bp from the start. The coverage was normalized to the number of million reads (RPM) by adding mean coverage. The IP data was then normalized to input data using the ratio operation in deepTools version 3.5.1. Next, the input normalized data were normalized to input normalized genomic DNA data using the ratio operation in deepTools. To make a direct comparison across all experiments, the data were Z-Score normalized using a custom R script (R version 3.6.1). Replicates were averaged using WiggleTools version 1.2.2. The profile plots were then made using deepTools.

Public dataset analysis (ChIP-seq profiles)

All normalized publicly available ChIP-seq and ChIP-chip data sets were lifted to the *C. elegans* reference genome version ce11, after which the replicates were averaged, and profiles were plotted using deepTools.

Hi-C analysis

Data from (Das et al., 2022; J. Kim et al., 2022; Morao et al., 2022) was processed using HiC-Pro at 2kb resolution and converted into balanced cool and mcool formats using cooler (Abdennur & Mirny, 2020). HiC data pileups and corresponding figures were created using GENOVA (van der Weide et al., 2021) in R. To account for the difference in resolution between HiC data (2 kb) and enhancer/TSS/HOT sites mappings (1 bp), the genome was tiled into 2kb bins. Enhancer locations with their annotation (active/repressed/H3K27me3) were taken from (Daugherty et al., 2017), lifted to ce11 and mapped to 2 kb bins. Consecutive or overlapping bins of the same type were merged before performing pileups. The overlap between non-identical type enhancers was minimal, with only 8, 98 and 34 active/H3K27me3, active/repressed and repressed/H3K27me3 bins, respectively, out of 2130, 1586 and 1483 active, H3K27me3 and repressed bins, respectively. The same

approach was taken for the (Jänes et al., 2018) enhancer list, except that the enhancer type was determined by mapping the enhancer locations to the ChromHMM chromatin states from (Evans et al., 2016). HiC data was loaded onto HiGlass for data exploration and ratio map creation (Kerpedjiev et al., 2018).

Inferring fountain positions and asymmetries

For each chromosome, fountain detection is based on the matrix *M* of log10 ratio between the WT and cohesin-depleted HiC maps (Fig. 2F). Based on a simple polymer model of loop extrusion, we defined a mask $F(\alpha_-,\alpha_+)$ where α_- and α_+ are related to the left and right extrusion speeds respectively and control the extent and asymmetry of the fountain (Fig. S3). First, we considered a symmetric mask $\alpha_- = \alpha_+ = \alpha_0$ and chose $\alpha_0 = 0.35$ to have a similar fountain size than those observed around enhancers (Fig. 1). We then computed for each position *i* along the genome the element-wise product matrix $fm(i)$ between $F(\alpha_0,\alpha_0)$ and *M* centered around *i*. The fountain score $S(i)$ is then defined as the mean value of the $fm(i)$ elements and $\sigma_S(i)$ as the standard error on $fm(i)$ elements (Fig. S3). We used the *find_peak* function of python package *scipy* to detect the peaks in the $S(i)$ profile. Peaks with a prominence larger than twice $\sigma_S(i)$ were considered as approximated fountain positions. To correct for possible asymmetry in fountain shapes that may alter the inference of the exact fountain position, we finally scanned around the approximated fountain position for the presence of asymmetric fountains by computing fountain scores for various asymmetric binarized masks $F(\alpha_-, 2\alpha_0 - \alpha_-)$ with $\alpha_- \in [0.05:0.05:2\alpha_0 - 0.05]$ ranging from left- to right-handed shapes (Fig. S3). From this, we estimated the exact position of the fountain and an asymmetry score ($\in$ [-1,1]) representing the degree of asymmetry of the fountain (<0: left-handed fountain, >0: right-handed fountain). All the details about mask definition, computation of fountain and asymmetry scores are given in a python *jupyter* notebook given in Supplementary Information.

Transcription inhibition experiments

Starting with 400,000 L3s in 10 ml M9 in a 50 ml falcon tube, added 200 µg/ml α-amanitin (Sigma-Aldrich) and OP50 that had been inactivated by heating at 65°C for 30 minutes. As a control, incubated the same amount of worms and inactivated OP-50 in the same volume with an equal volume of Milli-Q water. The reaction mixtures were incubated, rotating at room temperature in the dark for five hours. Spun the worms at 1000 rpm for 1 minute; the liquid was discarded, then washed the worms once with M9 and spun down at 1000 rpm for 1 minute. Resuspended the worms in 100 µl M9 with 200 µg/ml α-amanitin (for control, added Milli-Q water instead).

Fluorescent imaging of nematodes

Bleach-synchronized L1s were grown on OP-50 for 3 hours and then heat-shocked at 34°C for 30 minutes to induce TEV expression and COH-1 cleavage. L3 animals were collected 19 hours post-induction and anesthetized using 200 µl of 0.25 M levamisole. Worms were transferred on a 2 % agarose pad and imaged with a Nikon Ti2 microscope equipped with a Yokogawa spinning disk at 25°C. Z-stacks spaced by 0.3 µm covering 15 µm were acquired for GFP (488 nm), and the brightfield channel and maximum projections were merged in Fiji (Schindelin et al., 2012).

Microchambers preparation and growth analysis

Eggs from bleach synchronized parental culture were transferred into agarose-based arrayed 600 x 600 x 20 µm microchambers (Stojanovski, Großhans, et al., 2022), mounted onto a 3.5 cm gas permeable polymer dish (ibidi). Dishes were placed in a custom-made stage holder of a 22°C temperature-controlled Nikon Ti2 epifluorescence microscope equipped with a Hamamatsu ORCA Flash 4 sCMOS camera. Images were acquired with a 10x 0.45 NA objective every 10 minutes with 10 ms exposure time to minimize motion blur (Stojanovski, Gheorghe, et al., 2022), refocusing using Nikon's NIS software autofocus. Three hours after the start of time lapse imaging, the dish holder was removed from the microscope and dishes were subjected to a 30 minutes heat shock at 34°C to activate TEV expression. The dish holder was then mounted back onto the microscope and time lapse imaging restarted 75 minutes after dish removal. For the analysis, animals were selected which had hatched at least 150 minutes before heat-shock induction. Volume trajectories were determined using automated image analysis (Stojanovski, Gheorghe, et al., 2022) and manually curated for mistakes in molt annotation.

Behavioral analysis

Behavioral analysis was conducted at 22°C in young adult animals, as previously described (Thapliyal et al., 2023). Briefly, animals were synchronized and, except for N2 controls, submitted to a heat-shock to induce TEV expression as described above. Fed animals were maintained on 6-cm NGM plates with a lawn of OP50 bacteria. Food-deprived animals were deposited on unseeded NGM plates after 3 washes with distilled water. Several hours prior to experiments, plates were transferred into a custom-designed temperature- and vibration-controlled recording system. High resolution (2448×2048 pixels) 3-min movies of worm behavior (~50 animals/movie) were acquired with a DMK33UX250 camera (The Imaging Source), at 10 frames per second using IC Capture software (The Imaging Source). Movies were analyzed with the Tierpsy tracker (v1.4; (Javer et al., 2018) and we focused on a subset of 47 interpretable parameters, the choice of which was previously discussed

(Thapliyal et al., 2023). PCA and hierarchical clustering were performed with Clustvis webtool by default SVDimpute algorithm (Metsalu & Vilo, 2015). Each condition and genotype were recorded on at least 3 separate days with multiple replicates per day.

Comparative Gene Set Enrichment Analysis

Human-nematode orthologous genes were downloaded from Ortholist2 (W. Kim et al., 2018). Only orthologs that were detected by at least two programs were used in the analysis. A table of genes differentially expressed in Cornelia de Lange Syndrome neurons compared to control neurons (Weiss et al., 2021) was kindly provided by Matthias Merkenschlager. Genes were ranked by their Log2 fold change after COH-1 cleavage and their ranks used to test for enrichment of worm orthologs of significantly up and down regulated genes (padj<0.05) in CdLS patients using the fgsea package in R.

Supplementary data

Worm strains

Strain name	Genotype
PMW366	*ubsSi20[hsp-16.2p::TEV::unc-54 3'UTR; Cbr-unc-119(+)] II; unc-119(ed3) III*
PMW828	*ubsSi20[hsp-16.2p::TEV] II; unc-119(?) III; coh-1(ubs26[1xFLAG TEVcs]) X*
PMW836	*scc-1(ubs19[1xFLAG TEVcs]) ubsSi20[hsp-16.2p::TEV] II; unc-119(?) III; wIs54[scm::gfp] V*
PMW844	*scc-1(ubs19[1xFLAG TEVcs]) ubsSi20[hsp-16.2p::TEV] II; unc-119(?) III; coh-1(ubs26[1xFLAG TEVcs]) X*
PMW1116	*coh-1(ubs26[TEVcs]) X; ubsSi20[hsp-16.2p::TEV::unc-54 3'UTR; Cbunc-119] II ujIs113 II; skn-1(hq82([skn-1::gfp]) IV*
PMW1117	*coh-1(ubs26[TEVcs]) X; ujIs113 II; skn-1(hq82([skn-1::gfp]) IV*
PMW1063	*ubsSi20[hsp-16.2p::TEV::unc-54 3'UTR; Cbunc-119]II; xeSi301[Peft-3::luc::gfp::unc-54 3'UTR, unc-119(+)]III; coh-1(ubs26[TEVcs])X*
PMW1064	*ubsSi20[hsp-16.2p::TEV::unc-54 3'UTR; Cbunc-119]II; xeSi301[Peft-3::luc::gfp::unc-54 3'UTR, unc-119(+)]III*

Public datasets

Data set	Larval stage	GEO Accession code	Reference
RNAP II ChIP-seq	L3	GSE188851	(Morao et al., 2022)
TOP-1 ChIP-seq	L3	GSE188851	(Morao et al., 2022)
TOP-2 ChIP-seq	L3	GSE188851	(Morao et al., 2022)
COH-1 ChIP-seq	Young adult	modENCODE project	(Ho et al., 2014)
cohesin^{COH-1} cleavage Hi-C	L3	GSE199723	(Das et al., 2022)
Cohesin^{SCC-1} cleavage Hi-C	L3	GSE199723	(Das et al., 2022)
TIR1 control Hi-C	L3	GSE188851	(Morao et al., 2022)
TOP-1 Hi-C	L3	GSE188851	(Morao et al., 2022)
TOP-2 Hi-C	L3	GSE188851	(Morao et al., 2022)
cohesin^{COH-1} cleavage RNA-seq	L3	GSE199723	(Das et al., 2022)
Cohesin^{SCC-1} cleavage RNA-seq	L3	GSE199723	(Das et al., 2022)
Enhancers	L3	GSE114494	(Jänes et al., 2018)
Enhancers	L3	GSE89608	(Daugherty et al., 2017)
HOT regions	Late embryo	GSE49870	(Chen et al., 2014)

Supplementary files

Supplementary file 1.

Python script for fountain detection on ratio maps. (pdf and ipynb formats).

Supplementary file 2.

Bed format file with detected fountains genome-wide (result of supplementary file 1).

References

Abdennur, N., & Mirny, L. A. (2020). Cooler: scalable storage for Hi-C data and other genomically labeled arrays. *Bioinformatics* , *36*(1), 311–316.

Anderson, E. C., Frankino, P. A., Higuchi-Sanabria, R., Yang, Q., Bian, Q., Podshivalova, K., Shin, A., Kenyon, C., Dillin, A., & Meyer, B. J. (2019). X Chromosome Domain Architecture Regulates Caenorhabditis elegans Lifespan but Not Dosage Compensation. *Developmental Cell*, *51*(2), 192–207.e6.

Angeles-Albores, D., N Lee, R. Y., Chan, J., & Sternberg, P. W. (2016). Tissue enrichment analysis for C. elegans genomics. *BMC Bioinformatics*, *17*(1), 366.

Banigan, E. J., Tang, W., van den Berg, A. A., Stocsits, R. R., Wutz, G., Brandão, H. B., Busslinger, G. A., Peters, J.-M., & Mirny, L. A. (2022). Transcription shapes 3D chromatin organization by interacting with loop-extruding cohesin complexes. In *bioRxiv* (p. 2022.01.07.475367). https://doi.org/10.1101/2022.01.07.475367

Bian, Q., Anderson, E. C., Yang, Q., & Meyer, B. J. (2020). Histone H3K9 methylation promotes formation of genome compartments in *Caenorhabditis elegans* via chromosome compaction and perinuclear anchoring. In *Proceedings of the National Academy of Sciences* (Vol. 117, Issue 21, pp. 11459–11470). https://doi.org/10.1073/pnas.2002068117

Blackwell, T. K., Steinbaugh, M. J., Hourihan, J. M., Ewald, C. Y., & Isik, M. (2015). SKN-1/Nrf, stress responses, and aging in Caenorhabditis elegans. *Free Radical Biology & Medicine*, *88*(Pt B), 290–301.

Brandão, H. B., Paul, P., van den Berg, A. A., Rudner, D. Z., Wang, X., & Mirny, L. A. (2019). RNA polymerases as moving barriers to condensin loop extrusion. *Proceedings of the National Academy of Sciences of the United States of America*, *116*(41), 20489–20499.

Cheng, H., Zhang, N., & Pati, D. (2020). Cohesin subunit RAD21: From biology to disease. *Gene*, *758*, 144966.

Chen, R. A.-J., Stempor, P., Down, T. A., Zeiser, E., Feuer, S. K., & Ahringer, J. (2014). Extreme HOT regions are CpG-dense promoters in *C. elegans* and humans. In *Genome Research* (Vol. 24, Issue 7, pp. 1138–1146). https://doi.org/10.1101/gr.161992.113

Crane, E., Bian, Q., McCord, R. P., Lajoie, B. R., Wheeler, B. S., Ralston, E. J., Uzawa, S., Dekker, J., & Meyer, B. J. (2015). Condensin-driven remodelling of X chromosome topology during dosage compensation. *Nature*, *523*(7559), 240–244.

Crawley, O., Barroso, C., Testori, S., Ferrandiz, N., Silva, N., Castellano-Pozo, M., Jaso-Tamame, A. L., & Martinez-Perez, E. (2016). Cohesin-interacting protein WAPL-1 regulates meiotic chromosome structure and cohesion by antagonizing specific cohesin complexes. *eLife*, *5*, e10851.

Das, M., Semple, J. I., Volodkina, V., Haemmerli, A., Scotton, J., Gitchev, T., Annan, A., Statzer, C., Ewald, C. Y., Mozziconacci, J., Campos, J., & Meister, P. (2022). *Condensin I folds the C. elegans genome*. https://www.biorxiv.org/content/10.1101/2022.06.14.495661v1

Daugherty, A. C., Yeo, R. W., Buenrostro, J. D., Greenleaf, W. J., Kundaje, A., & Brunet, A. (2017). Chromatin accessibility dynamics reveal novel functional enhancers in C. elegans. *Genome Research*, *27*(12), 2096–2107.

Davidson, I. F., Bauer, B., Goetz, D., Tang, W., Wutz, G., & Peters, J.-M. (2019). DNA loop extrusion by human cohesin. *Science*, *366*(6471), 1338–1345.

Dixon, J. R., Selvaraj, S., Yue, F., Kim, A., Li, Y., Shen, Y., Hu, M., Liu, J. S., & Ren, B. (2012). Topological domains in mammalian genomes identified by analysis of chromatin interactions. *Nature*, *485*(7398), 376–380.

Evans, K. J., Huang, N., Stempor, P., Chesney, M. A., Down, T. A., & Ahringer, J. (2016). Stable Caenorhabditis elegans chromatin domains separate broadly expressed and developmentally regulated genes. *Proceedings of the National Academy of Sciences of the United States of America*, *113*(45), E7020–E7029.

Flavell, S. W., Raizen, D. M., & You, Y.-J. (2020). Behavioral States. *Genetics*, *216*(2), 315–332.

Fujita, Y., Masuda, K., Bando, M., Nakato, R., Katou, Y., Tanaka, T., Nakayama, M., Takao, K., Miyakawa, T., Tanaka, T., Ago, Y., Hashimoto, H., Shirahige, K., & Yamashita, T. (2017). Decreased cohesin in the brain leads to defective synapse development and anxiety-related behavior. *The Journal of Experimental Medicine*, *214*(5), 1431–1452.

Galitsyna, A., Ulianov, S. V., Bykov, N., Veil, M., Gao, M., Perevoschikova, K., Gelfand, M., Razin, S. V., Mirny, L., & Onichtchouk, D. (2023). Extrusion fountains are hallmarks of chromosome organization emerging upon zygotic genome activation. *bioRxiv*.

Gerstein, M. B., Lu, Z. J., Van Nostrand, E. L., Cheng, C., Arshinoff, B. I., Liu, T., Yip, K. Y., Robilotto, R., Rechtsteiner, A., Ikegami, K., Alves, P., Chateigner, A., Perry, M., Morris, M., Auerbach, R. K., Feng, X., Leng, J., Vielle, A., Niu, W., … Waterston, R. H. (2010). Integrative analysis of the Caenorhabditis elegans genome by the modENCODE project. *Science*, *330*(6012), 1775–1787.

Golfier, S., Quail, T., Kimura, H., & Brugués, J. (2020). Cohesin and condensin extrude DNA loops in a cell cycle-dependent manner. *eLife*, *9*. https://doi.org/10.7554/eLife.53885

Guo, Y., Al-Jibury, E., Garcia-Millan, R., Ntagiantas, K., King, J. W. D., Nash, A. J., Galjart, N., Lenhard, B., Rueckert, D., Fisher, A. G., Pruessner, G., & Merkenschlager, M. (2022). Chromatin jets define the properties of cohesin-driven in vivo loop extrusion. *Molecular Cell*, *82*(20), 3769–3780.e5.

Han, R., Huang, Y., Vaandrager, I., Allahyar, A., Magnitov, M., Verstegen, M. J. A., de Wit, E., Krijger, P. H. L., & de Laat, W. (2023). Targeted cohesin loading characterizes the entry and exit sites of loop extrusion trajectories. In *bioRxiv* (p. 2023.01.04.522689). https://doi.org/10.1101/2023.01.04.522689

Ho, J. W. K., Jung, Y. L., Liu, T., Alver, B. H., Lee, S., Ikegami, K., Sohn, K.-A., Minoda, A., Tolstorukov, M. Y., Appert, A., Parker, S. C. J., Gu, T., Kundaje, A., Riddle, N. C., Bishop, E., Egelhofer, T. A., Hu, S. S., Alekseyenko, A. A., Rechtsteiner, A., … Park, P. J. (2014). Comparative analysis of metazoan chromatin organization. *Nature*, *512*(7515), 449–452.

Holdorf, A. D., Higgins, D. P., Hart, A. C., Boag, P. R., Pazour, G. J., Walhout, A. J. M., &

Walker, A. K. (2020). WormCat: An Online Tool for Annotation and Visualization of Caenorhabditis elegans Genome-Scale Data. *Genetics*, *214*(2), 279–294.

Jänes, J., Dong, Y., Schoof, M., Serizay, J., Appert, A., Cerrato, C., Woodbury, C., Chen, R., Gemma, C., Huang, N., Kissiov, D., Stempor, P., Steward, A., Zeiser, E., Sauer, S., & Ahringer, J. (2018). Chromatin accessibility dynamics across C. elegans development and ageing. *eLife*, *7*. https://doi.org/10.7554/eLife.37344

Javer, A., Ripoll-Sánchez, L., & Brown, A. E. X. (2018). Powerful and interpretable behavioural features for quantitative phenotyping of Caenorhabditis elegans. *Philosophical Transactions of the Royal Society of London. Series B, Biological Sciences*, *373*(1758), 20170375.

Jimenez, D. S., Kim, J., Ragipani, B., Zhang, B., & Street, L. A. (2021). Condensin DC spreads linearly and bidirectionally from recruitment sites to create loop-anchored TADs in C. elegans. *bioRxiv*. https://www.biorxiv.org/content/10.1101/2021.03.23.436694v1.abstract

Karpinska, M. A., & Oudelaar, A. M. (2023). The role of loop extrusion in enhancer-mediated gene activation. *Current Opinion in Genetics & Development*, *79*(102022), 102022.

Kerpedjiev, P., Abdennur, N., Lekschas, F., McCallum, C., Dinkla, K., Strobelt, H., Luber, J. M., Ouellette, S. B., Azhir, A., Kumar, N., Hwang, J., Lee, S., Alver, B. H., Pfister, H., Mirny, L. A., Park, P. J., & Gehlenborg, N. (2018). HiGlass: web-based visual exploration and analysis of genome interaction maps. In *Genome Biology* (Vol. 19, Issue 1). https://doi.org/10.1186/s13059-018-1486-1

Kim, J., Jimenez, D. S., Ragipani, B., Zhang, B., Street, L. A., Kramer, M., Albritton, S. E., Winterkorn, L. H., Morao, A. K., & Ercan, S. (2022). Condensin DC loads and spreads from recruitment sites to create loop-anchored TADs in *C. elegans*. *eLife*, *11*. https://doi.org/10.7554/eLife.68745

Kim, W., Underwood, R. S., Greenwald, I., & Shaye, D. D. (2018). OrthoList 2: A New Comparative Genomic Analysis of Human and Caenorhabditis elegans Genes. *Genetics*, *210*(2), 445–461.

Kline, A. D., Moss, J. F., Selicorni, A., Bisgaard, A.-M., Deardorff, M. A., Gillett, P. M., Ishman, S. L., Kerr, L. M., Levin, A. V., Mulder, P. A., Ramos, F. J., Wierzba, J., Ajmone, P. F., Axtell, D., Blagowidow, N., Cereda, A., Costantino, A., Cormier-Daire, V., FitzPatrick, D., … Hennekam, R. C. (2018). Diagnosis and management of Cornelia de Lange syndrome: first international consensus statement. *Nature Reviews. Genetics*, *19*(10), 649–666.

Latorre, I., Chesney, M. A., Garrigues, J. M., Stempor, P., Appert, A., Francesconi, M., Strome, S., & Ahringer, J. (2015). The DREAM complex promotes gene body H2A.Z for target repression. *Genes & Development*, *29*(5), 495–500.

Lehrbach, N. J., & Ruvkun, G. (2016). Proteasome dysfunction triggers activation of SKN-1A/Nrf1 by the aspartic protease DDI-1. *eLife*, *5*. https://doi.org/10.7554/eLife.17721

Liu, N. Q., Magnitov, M., Schijns, M., van Schaik, T., van der Weide, R. H., Teunissen, H., van Steensel, B., & de Wit, E. (2021). Rapid depletion of CTCF and cohesin proteins reveals dynamic features of chromosome architecture. In *bioRxiv* (p. 2021.08.27.457977). https://doi.org/10.1101/2021.08.27.457977

Meeuse, M. W., Hauser, Y. P., Morales Moya, L. J., Hendriks, G.-J., Eglinger, J., Bogaarts, G., Tsiairis, C., & Großhans, H. (2020). Developmental function and state transitions of a gene expression oscillator in Caenorhabditis elegans. *Molecular Systems Biology*, *16*(7), e9498.

Metsalu, T., & Vilo, J. (2015). ClustVis: a web tool for visualizing clustering of multivariate data using Principal Component Analysis and heatmap. *Nucleic Acids Research*, *43*(W1), W566–W570.

Mito, Y., Sugimoto, A., & Yamamoto, M. (2003). Distinct developmental function of two Caenorhabditis elegans homologs of the cohesin subunit Scc1/Rad21. *Molecular Biology of the Cell*, *14*(6), 2399–2409.

Morao, A. K., Kim, J., Obaji, D., Sun, S., & Ercan, S. (2022). Topoisomerases I and II facilitate condensin DC translocation to organize and repress X chromosomes in C.

elegans. *Molecular Cell*, *82*(22), 4202–4217.e5.

Naughton, C., Avlonitis, N., Corless, S., Prendergast, J. G., Mati, I. K., Eijk, P. P., Cockroft, S. L., Bradley, M., Ylstra, B., & Gilbert, N. (2013). Transcription forms and remodels supercoiling domains unfolding large-scale chromatin structures. *Nature Structural & Molecular Biology*, *20*(3), 387–395.

Parenti, I., & Kaiser, F. J. (2021). Cornelia de Lange Syndrome as Paradigm of Chromatinopathies. *Frontiers in Neuroscience*, *15*, 774950.

Pasierbek, P., Jantsch, M., Melcher, M., Schleiffer, A., Schweizer, D., & Loidl, J. (2001). A Caenorhabditis elegans cohesion protein with functions in meiotic chromosome pairing and disjunction. *Genes & Development*, *15*(11), 1349–1360.

Pauli, A., Althoff, F., Oliveira, R. A., Heidmann, S., Schuldiner, O., Lehner, C. F., Dickson, B. J., & Nasmyth, K. (2008). Cell-type-specific TEV protease cleavage reveals cohesin functions in Drosophila neurons. *Developmental Cell*, *14*(2), 239–251.

Pueschel, R., Coraggio, F., & Meister, P. (2016). From single genes to entire genomes: the search for a function of nuclear organization. *Development* , *143*(6), 910–923.

Rao, S. S. P., Huang, S.-C., Glenn St Hilaire, B., Engreitz, J. M., Perez, E. M., Kieffer-Kwon, K.-R., Sanborn, A. L., Johnstone, S. E., Bascom, G. D., Bochkov, I. D., Huang, X., Shamim, M. S., Shin, J., Turner, D., Ye, Z., Omer, A. D., Robinson, J. T., Schlick, T., Bernstein, B. E., … Aiden, E. L. (2017). Cohesin Loss Eliminates All Loop Domains. *Cell*, *171*(2), 305–320.e24.

Rinzema, N. J., Sofiadis, K., Tjalsma, S. J. D., Verstegen, M. J. A. M., Oz, Y., Valdes-Quezada, C., Felder, A.-K., Filipovska, T., van der Elst, S., de Andrade Dos Ramos, Z., Han, R., Krijger, P. H. L., & de Laat, W. (2022). Building regulatory landscapes reveals that an enhancer can recruit cohesin to create contact domains, engage CTCF sites and activate distant genes. *Nature Structural & Molecular Biology*, *29*(6), 563–574.

Rivosecchi, J., Jost, D., Vachez, L., Gautier, F. D., Bernard, P., & Vanoosthuyse, V. (2021). RNA polymerase backtracking results in the accumulation of fission yeast condensin at

active genes. *Life Science Alliance*, *4*(6). https://doi.org/10.26508/lsa.202101046

Robles-Rebollo, I., Cuartero, S., Canellas-Socias, A., Wells, S., Karimi, M. M., Mereu, E., Chivu, A. G., Heyn, H., Whilding, C., Dormann, D., Marguerat, S., Rioja, I., Prinjha, R. K., Stumpf, M. P. H., Fisher, A. G., & Merkenschlager, M. (2022). Cohesin couples transcriptional bursting probabilities of inducible enhancers and promoters. *Nature Communications*, *13*(1), 4342.

Schindelin, J., Arganda-Carreras, I., Frise, E., Kaynig, V., Longair, M., Pietzsch, T., Preibisch, S., Rueden, C., Saalfeld, S., Schmid, B., Tinevez, J.-Y., White, D. J., Hartenstein, V., Eliceiri, K., Tomancak, P., & Cardona, A. (2012). Fiji: an open-source platform for biological-image analysis. *Nature Methods*, *9*(7), 676–682.

Schwarzer, W., Abdennur, N., Goloborodko, A., Pekowska, A., Fudenberg, G., Loe-Mie, Y., Fonseca, N. A., Huber, W., Haering, C. H., Mirny, L., & Spitz, F. (2017). Two independent modes of chromatin organization revealed by cohesin removal. *Nature*, *551*(7678), 51–56.

Stojanovski, K., Gheorghe, I., Lanjuin, A., Mair, W. B., & Towbin, B. D. (2022). Ultra-sensitive coupling between organ growth and size by YAP-1 ensures uniform body plan proportions in C. elegans. In *bioRxiv* (p. 2022.09.05.506666). https://doi.org/10.1101/2022.09.05.506666

Stojanovski, K., Großhans, H., & Towbin, B. D. (2022). Coupling of growth rate and developmental tempo reduces body size heterogeneity in C. elegans. *Nature Communications*, *13*(1), 3132.

Takagi, S., Bénard, C., Pak, J., Livingstone, D., & Hekimi, S. (1997). Cellular and axonal migrations are misguided along both body axes in the maternal-effect mau-2 mutants of Caenorhabditis elegans. *Development* , *124*(24), 5115–5126.

Tataridas-Pallas, N., Thompson, M. A., Howard, A., Brown, I., Ezcurra, M., Wu, Z., Silva, I. G., Saunter, C. D., Kuerten, T., Weinkove, D., Blackwell, T. K., & Tullet, J. M. A. (2021). Neuronal SKN-1B modulates nutritional signalling pathways and mitochondrial networks to control satiety. *PLoS Genetics*, *17*(3), e1009358.

Teuscher, A. C., & Ewald, C. Y. (2018). Overcoming Autofluorescence to Assess GFP Expression During Normal Physiology and Aging in Caenorhabditis elegans. *Bio-Protocol*, *8*(14). https://doi.org/10.21769/BioProtoc.2940

Thapliyal, S., Beets, I., & Glauser, D. A. (2023). Multisite regulation integrates multimodal context in sensory circuits to control persistent behavioral states in C. elegans. *Nature Communications*, *14*(1), 3052.

Tran, N. T., Laub, M. T., & Le, T. B. K. (2017). SMC Progressively Aligns Chromosomal Arms in Caulobacter crescentus but Is Antagonized by Convergent Transcription. *Cell Reports*, *20*(9), 2057–2071.

Tullet, J. M. A., Hertweck, M., An, J. H., Baker, J., Hwang, J. Y., Liu, S., Oliveira, R. P., Baumeister, R., & Blackwell, T. K. (2008). Direct inhibition of the longevity-promoting factor SKN-1 by insulin-like signaling in C. elegans. *Cell*, *132*(6), 1025–1038.

van der Weide, R. H., van den Brand, T., Haarhuis, J. H. I., Teunissen, H., Rowland, B. D., & de Wit, E. (2021). Hi-C analyses with GENOVA: a case study with cohesin variants. *NAR Genomics and Bioinformatics*, *3*(2), lqab040.

Weiss, F. D., Calderon, L., Wang, Y.-F., Georgieva, R., Guo, Y., Cvetesic, N., Kaur, M., Dharmalingam, G., Krantz, I. D., Lenhard, B., Fisher, A. G., & Merkenschlager, M. (2021). Neuronal genes deregulated in Cornelia de Lange Syndrome respond to removal and re-expression of cohesin. *Nature Communications*, *12*(1), 2919.

Wike, C. L., Guo, Y., Tan, M., Nakamura, R., Shaw, D. K., Díaz, N., Whittaker-Tademy, A. F., Durand, N. C., Aiden, E. L., Vaquerizas, J. M., Grunwald, D., Takeda, H., & Cairns, B. R. (2021). Chromatin architecture transitions from zebrafish sperm through early embryogenesis. *Genome Research*, *31*(6), 981–994.

Wutz, G., Várnai, C., Nagasaka, K., Cisneros, D. A., Stocsits, R. R., Tang, W., Schoenfelder, S., Jessberger, G., Muhar, M., Hossain, M. J., Walther, N., Koch, B., Kueblbeck, M., Ellenberg, J., Zuber, J., Fraser, P., & Peters, J.-M. (2017). Topologically associating domains and chromatin loops depend on cohesin and are regulated by CTCF, WAPL, and PDS5 proteins. *The EMBO Journal*, *36*(24), 3573–3599.

Zuin, J., Roth, G., Zhan, Y., Cramard, J., Redolfi, J., Piskadlo, E., Mach, P., Kryzhanovska, M., Tihanyi, G., Kohler, H., Eder, M., Leemans, C., van Steensel, B., Meister, P., Smallwood, S., & Giorgetti, L. (2022). Nonlinear control of transcription through enhancer–promoter interactions. *Nature*, *604*(7906), 571–577.